INVESTIGATION OF DUAL-NARROWBAND PLASMONIC PERFECT ABSORBERS AT VISIBLE FREQUENCIES FOR BIOSENSING

A THESIS SUBMITTED TO

THE GRADUATE SCHOOL OF ENGINEERING AND SCIENCE

OF BILKENT UNIVERSITY

IN PARTIAL FULFILLMENT OF THE REQUIREMENTS FOR

THE DEGREE OF

MASTER OF SCIENCE

IN

PHYSICS

By

Farhan Ali

December 2019

Investigation of dual-narrowband plasmonic perfect absorbers at visible frequencies for biosensing
By Farhan Ali
December 2019

We certify that we have read this thesis and that in our opinion it is fully adequate, in scope and in quality, as a thesis for the degree of Master of Science.

Oğuz Gülseren(Advisor)

Serap Aksu(Co-Advisor)

Bilal Tanatar

Selçuk Yerci

Approved for the Graduate School of Engineering and Science:

Ezhan Karaşan
Director of the Graduate School

ABSTRACT

INVESTIGATION OF DUAL-NARROWBAND PLASMONIC PERFECT ABSORBERS AT VISIBLE FREQUENCIES FOR BIOSENSING

Farhan Ali
M.S. in Physics
Advisor: Oğuz Gülseren
Co-Advisor: Serap Aksu
December 2019

Since the introduction of first plasmonic perfect absorber (PA) in early 2008 by Landy et al., numerous studies have demonstrated their superior optical performance in frequencies ranging from terahertz to visible region of electromagnetic spectrum. In the literature broadband PAs are studied in more detail compared to narrowband PAs as their large absorption bandwidths make them a prime candidate for energy harvesting applications or security and defense. Recently scientists have shown a great interest in designing narrowband PAs by controlling the optical losses of the plasmonic materials as the narrowband resonances with a high quality-factor is particularly important for label-free biosensing. However, given the lossy optical properties of metals, this task has been challenging and requires delicate investigation and parameter control in contrast to broadband perfect absorbers.

In this research, we numerically studied and experimentally fabricated a narrow-band plasmonic perfect absorber based on a metal-insulator-metal configuration. We analyzed the origin of perfect absorption for our proposed system and investigated the parameters that effect the optical properties. The purposed plasmonic structure comes up with a dual narrow-band absorption peaks at visible and near-infrared region of electromagnetic spectrum with near unity absorption efficiency. The physical origin of these absorption peaks is shown to be the excitation of propagating and localized surface plasmon resonances at certain individual frequencies, that leads to impedance matching and critical coupling when certain conditions are satisfied.

Finally, we analyzed the sensing capabilities of PA by embedding nanostructure into different background refractive index, resulting in sensitivity of 500 nm/RIU, making such a platform suitable for biosensing and spectroscopic applications.

This work analyzes the perfect absorption phenomena in visible frequencies in detail and will be a go to guide for researchers in the perfect absorber community.

Keywords: Plasmonic nanostructures, Metamaterial, MIM Perfect absorber, Narrowband perfect absorbers, Biosensing.

ÖZET

BİYO ALGILAMA İÇİN GÖRÜLEBİLİR FREKANSLARDA İKİLİ İNCE BANT PLAZMONİK MÜKEMMEL SOĞURUCULARI İNCELEMESİ

Farhan Ali
Fizik, Yüksek Lisans
Tez Danışmanı: Oğuz Gülseren
İkinci Tez Danışmanı: Serap Aksu
Aralık 2019

Ilk plazmonik mükemmel soğurucu (MS) tanıtıldığından beri birçok çalışma terahertzden görülebilir frekanslara kadar çalışabilen bu malzemelerin üstün optik performanslarını göstermek üzere sunulmuştur. Bunlar arasında geniş bantta absopsiyon gösteren MSler, yüksek soğurma genişliklerinden dolayı enerji hasatı, güvenlik ve savunma alanındaki uygulamalarda sıklıkla kullanılmıştır. Son zamanlarda bilim insanları, yüksek kalite faktörüne sahip ince bant rezonanslarının işaretsiz biyo algılamadaki öneminden dolayı ince bant MS tasarımına yüksek ilgi göstermişlerdir. Ancak metallerin optik kayıplarından dolayı geniş bant mükemmel soğurucuların aksine ince-bantların elde edilmesi hassas ve belirli parametrelerin kontrolünü gerektirmektedir.

Bu çalışmada metal-yalıtkan-nano metal yapılı bir ince bant plazmonik mükemmel soğurucusunu deneysel olarak üretip nümerik olarak optik performansını araştırdık. Önerilen sistemdeki mükemmel soğurmanın kökenini inceledik ve optik özellikleri etkileyen parametreleri belirledik. Hedeflenen plazmonik yapı tam soğurma verimi ile elektromanyetik spektrumun görülebilir ve yakın kızılötesi bölgesinde ikili rezonans frekansı oluşturmaktadır. Söz konusu soğurma rezonansının fiziksel kökeninin yayılan ve lokal yüzey plazmon rezonasının belirli frekanslarda uyarılması, bunun da belirli koşullar altında empedans eşleşmesi ve kritik eşleşmeye sebep olması olduğu gösterildi.

Son olarak, MSnin algılama kapsitesi nanoyapının faklı kırma indekslerindeki resonansları ile analiz edildi, ve belirlenen hassasiyetin (500 nm/RIU) platformun biyo algılama ve spektroskopik uygulamalar için uygun olduğu gösterildi.

Bu çalışma, görülebilir frekanslardaki mükemmel soğurma olayını detaylıca araştırmış, ve mükemmel soğurma alanında çalışanlar için güvenilir bir rehber olmuştur.

Anahtar sözcükler: Plazmonik nanoyapılar,Metamateryal, MYM Mükemmel Soğurucu, Ince bant Mükemmel Soğurucular, Biyo algılama. .

Acknowledgement

First of all, I would like to express my deep gratitude to my advisor, Dr. Serap Aksu for her extensive guidance and support throughout this research period. It's all of her trust and motivation which helped me to focus on my work despite of a lot of challenges and roadblocks. I am grateful for all the support i received, her patience and knowledge she shared to make this thesis possible. I would also like to thank Prof. Oğuz Gülseren for his support and help.

I acknowledge Semih Korkmaz (PhD scholar at Erciyes University, Turkey) who helped me to understand this field in the very beginning. I am also extremely thankful to my friends and colleagues Luqman Saleem (PhD scholar at KAUST, Saudi Arabia), Mohammad Hilal, Mohammad Sallahuddin,Ali Sheraz, Samar Batool, Naveed Mehmood, Sabeeh Iqbal (Graduae scholars at Bilkent University), and Armagan Ayaz (PhD scholar at Koç University), for the motivation and meaningful discussions about my research work. I am grateful to Umutcan Güler, MS student at Physics department, who translated abstract into Turkish.

I own more than thanks to my family and friends back in Pakistan for all kind of support and encouragement. Especially my brothers for supporting my decisions and believing in me while i didn't. They have a huge role in all of my achievements till date. Finally I dedicate my thesis to my parents, especially to my beloved father, Naseer Ahmed who is not here with us now, but would have been very happy on this achievement of mine.

I acknowledge financial support by TÜBİTAK under project no. 117F345.

Contents

List of Figures

List of Tables

Chapter 1

Introduction

1.1 Motivation

Since the last decade, Plasmonics, a field laying at the interface of Photonics, electronics and nanotechnology, has been able to caught researchers attention due to its potential control of light matter interaction at sub-wavelength scale [1, 2]. Plasmonics take benefit from the collective oscillations of conduction electrons (Plasmons) at metallic interfaces, and to create possibilities of coupling of electromagnetic radiation with nanoscale objects resulting in the generation of a broad range of novel optical phenomenons at sub-wavelength scale. Confinement of light at nanoscale, strong electromagnetic field enhancements, scattering and absorption at resonance are among the most remarkable properties exploited by it [3]. These unique and unordinary properties allow it to cover a wide range of novel stimulating applications in the fields of biomedicine, nanoelectronics, photocatalyis, photovoltaics and many more. Bio-sensors, nanolasers, photo-detectors, optical filters, absorbers are some of its exciting applications in above mentioned fields of study [4, 5, 6, 7, 8].

Among the most rapidly growing fields of research in recent years, electromagnetic metamaterials (MM) is also the one, which takes advantage from the composition of naturally existing materials in such a way that they deliver exotic electromagnetic properties, which are unachievable in the nature [9]. These artificial materials consist of sub-wavelength structures and can be treated as a homogeneous medium with an effective permittivity (ϵ) and permeability (μ), allowing to tune these materials deliberately thus yielding unusual properties like negative refractive index materials. Such exotic properties enable such materials to produce many exciting and fascinating applications like perfect lenses, electromagnetic invisibility cloaking and MM perfect absorbers [10, 11, 12].

Plasmonic metamaterial perfect absorbers (PAs) have gained much attention since the first PA proposed in early 2008 by Landy et al. [13] due to its high efficiency to absorb incident electromagnetic energy, and numerous efforts have been made to study PAs from terahertz to visible region of electromagnetic spectrum. In the literature, broadband PAs are investigated in more details than narrowband PAs due to its large absorption bandwidths, which make such an absorber ideal candidate for energy harvesting and security purposes [14, 15]. However, in recent years scientists have also shown a great interest in designing narrowband PAs by excitation of narrowband resonances with high quality-factor, and employing them for spectroscopic and sensing applications [16, 17, 18]. Most of these narrowband PA are uni-resonant, but a delicate control over structural parameters lead to multi-resonant PAs [19, 20, 21]. Researchers comes up with different platforms based PA, among which the most typical one is based on a Metal-Insulator-Metal (MIM) platforms, where a sheet of insulating spacer is sandwiched between a bottom metallic plate and a top periodic metallic patterned layer serving as nanoantennas [22]. Also, most of the Multi-resonant PAs are reported in the Infrared region, but to best of our knowledge no MIM platform based PA is proposed yet with a proper study both numerically and experimentally at viable-near-Infrared frequencies for biosensing applications. So, here our aim is to fill the gap at these frequencies.

1.2 Project Overview

This project is aimed to design, simulate and fabricate a dual-narrowband plasmonic perfect absorber at visible frequencies for biosensing applications. This research work is carried out through a cycle of steps shown in Fig. 1.1.

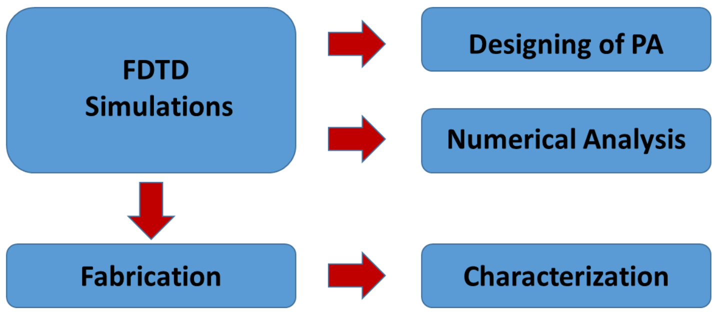

Figure 1.1: Project cycle : A schematics of the steps followed to carry out this research work.

In the first step, finite difference time domain (FDTD) method is employed to design a narrowband PA based on a MIM configuration, and from an iterative simulation analysis, the device giving maximum efficiency is chosen to further analyze the system. In the next step, similar method is applied to numerically investigate the physical mechanism of the PA and its performance relationship with various parameters of the system. After a successful numerical analysis, the designed PA is fabricated and characterized using standard nanofabrication and characterization techniques. Finally, the sensing capabilities of the PA are described to show that it can be a prime candidate for spectroscopic and biosensing applications.

1.3 Theoretical background

Fundamental light matter interaction results in some interesting phenomenons. Surface Plasmons (SPs) is one of them, where free electrons in metals oscillate collectively at the metal-dielectric interface under certain conditions. Excitation of these surface plasmons is usually described a technique, so called Surface Plasmon Resonance (SPR). When an electromagnetic radiation is incident on noble metal nanoparticles, a sea of conduction electrons above metal surface starts oscillating coherently relative to a lattice of positive ion cores, leading to displace the electronic cloud from the nuclei. consequently, there is a surface charge distribution. Due to charge separation between displaced electronic cloud and positive background, a restoring force is induced. These forces give rise to periodic collective oscillation associated to different surface charge distributions, known as Surface Plasmon Resonance (SPR). Surface Plasmon Resonance is categorized into two main classes: Surface Plasmon Polariton (SPP) and Localized Surface Plasmon resonance (LSPR) [1, 23].

Surface Plasmon Polaritons (SPPs) are the non-stationary excitations propagating along metal-dielectric interface and decay exponentially upto 200 nm in a direction perpendicular to the propagation. These modes arise due to coupling of light with plasmons under certain conditions. SPP cannot be excited directly by illumination of light as there is a momentum mismatch between wavevector of SPP and dispersion relation of light in free space as shown in figure 1.2. To overcome this problem, techniques like prism coupling (kretschmann configuration) and grating coupling (Periodic structures) are used to provide additional wavevector to conserve momentum and excite SPP. On the other hand, Localized Surface Plasmons (LSPs) are the stationary excitations of free conduction electrons coupled to electromagnetic field. Localized Surface Plasmon Resonance (LSPR) can be excited directly by incident electromagnetic radiation on nanoparticles as a result of scattering and absorption through the surface of the sub-wavelength sized conductive particles shown by figure 1.2. Such kind of Resonance is strongly dependent on geometrical parameters, composition as well as surrounding environment of the particle [24, 25].

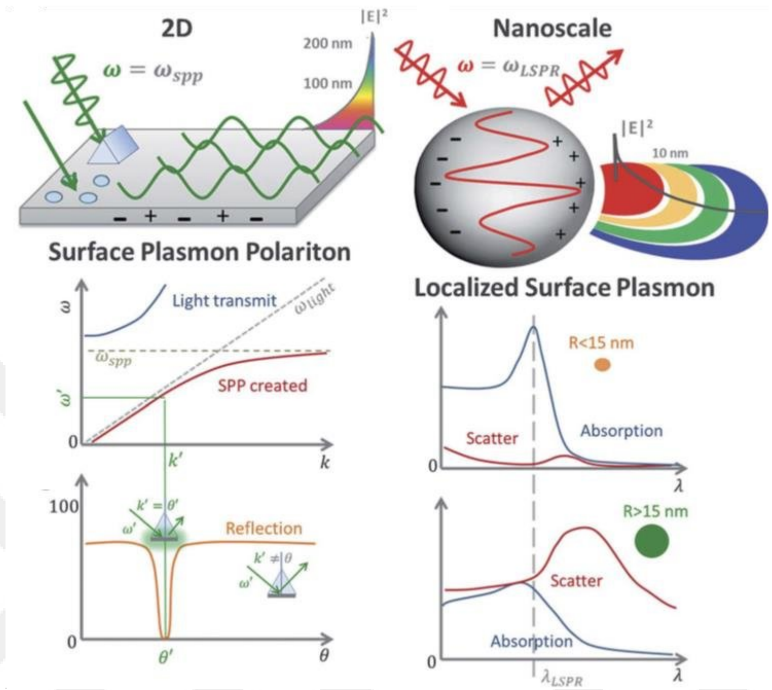

Figure 1.2: A comparison of Surface Plasmon Polariton and Localized Surface Plasmon Resonance [25].

1.3.1 Maxwell's Equations

To investigate the optical properties of metals, we usually take advantage of Maxwell's equations which are the basic pillars of classical electrodynamics given as

$$\nabla \cdot \vec{D} = \rho_{ext} \tag{1.1}$$

$$\nabla \cdot \vec{B} = 0 \tag{1.2}$$

$$\nabla \times \vec{E} = -\frac{\partial \vec{B}}{\partial t} \tag{1.3}$$

$$\nabla \times \vec{H} = J_{ext} + \frac{\partial \vec{D}}{\partial t} \tag{1.4}$$

These equations describe macroscopic fields and how they are linked with each other. In equations (1.1-1.4), external charge density ρ_{ext} and current density

J_{ext} are Electric and magnetic field sources, respectively. D and E are electric field displacement and electric field intensity, whereas H and B are magnetic field intensity and magnetic induction. From Maxwell's equation, electric displacement $\vec{D}$ and Magnetic induction $\vec{B}$ in a material with material constants ϵ, μ are associated with the electric field intensity$\vec{E}$ and magnetic field intensity$\vec{H}$ as

$$\vec{D} = \epsilon\vec{E} = \epsilon_0\vec{E} + \vec{P} \tag{1.5}$$

$$\vec{B} = \mu\vec{H} = \mu_0(\vec{H} + \vec{M}) \tag{1.6}$$

where, $\vec{P}$ is electric polarization vector, $\vec{M}$ is magnetic polarization vector and ϵ_0, μ_0 are permittivity and permeability of free space.

1.3.2 Dielectric Function of free electrons gas and Inter-band transitions

Drude model is widely used to understand the response of a metal to any external electromagnetic field by describing the behavior of its conduction electrons. Paul Drude presented this model in 1900, which assume that the conduction electrons are free and can move similar to an electron gas. These free electrons collide with each other and the ions with a collision frequency $\gamma = 1/\tau$, where τ is known as relaxation time. In a consequence to these collision, these electrons can also come out of the metallic surface and form a sea of electrons above the surface moving with a specific frequency, known as Plasma frequency (ω_p). By adopting the so called Drude-Sommerfeld model, one can write the equation of motion for a free conduction electron as

$$m\frac{\partial^2\mathbf{r}}{\partial t^2} + m\gamma\frac{\partial\ \mathbf{r}}{\partial t} = -e\mathbf{E}(t) \tag{1.7}$$

where m, e are mass and charge of an electron, E(t) is time dependent incident electromagnetic field. By doing simple Fourier transformation in time domain, one can reach the solution to $\mathbf{r}$ in frequency space as

$$\mathbf{r}(\omega) = \frac{e^2/m}{\omega^2 + i\gamma\omega}\mathbf{E}(\omega) \tag{1.8}$$

with i being the sign of imaginary unit. Now, we can define electric polarization vector, dipole moment per unit volume, by $\mathbf{P}$ = -ne$\mathbf{r}(\omega)$, where n is the density of electrons.

Now, by inserting the above mentioned value of $\mathbf{P}$ in equation(1.5) and combining with (1.8), it is quite easy to reach the dielectric function of the free electrons given by

$$\epsilon(\omega) = 1 - \frac{\omega_p^2}{\omega^2 + i\gamma\omega} \tag{1.9}$$

where $\omega_p = \sqrt{\frac{ne^2}{\epsilon_0 m}}$ is the plasma frequency. This complex dielectric function is divided into real and imaginary parts as $\epsilon(\omega) = \epsilon_R(\omega) + i\epsilon_I(\omega)$ given by

$$\epsilon_R(\omega) = 1 - \frac{\omega_p^2\tau^2}{1 + \omega^2\tau^2} \tag{1.10a}$$

$$\epsilon_I(\omega) = \frac{\omega_p^2\tau^2}{\omega(1 + \omega^2\tau^2)} \tag{1.10b}$$

We can further study dispersion relation for the dielectric function of free electron gas in different frequency regimes. In the regime $\omega < \omega_p$, when the frequency reaches near plasma frequency, there is negligible damping as the product, $\omega\tau$, becomes too smaller than the order of magnitude($\omega\tau << 1$). As a result, dielectric function can be rewritten as

$$\epsilon(\omega) = 1 - \frac{\omega_p^2}{\omega^2} \tag{1.11}$$

In the regime $\omega > \omega_p$, combining the equation (1.11) and general dispersion relation for transverse relation, $K^2 = \epsilon(\omega)(\omega/c)^2$, one can reach the dispersion relation given by

$$\omega^2 = \omega_p^2 + (Kc)^2 \tag{1.12}$$

and plotted in figure(1.3). We can see when the frequency of incidnet EM wave is less than plasma frequency, the propagation is forbidden. In contrast, for $\omega > \omega_p$ the wave is supported by plasma and propagates in the medium with a group velocity $v_g = d\omega/dK$.

The above mentioned Drude model works well to describe the optical properties of metals for the frequency range upto near IR. As we move toward higher

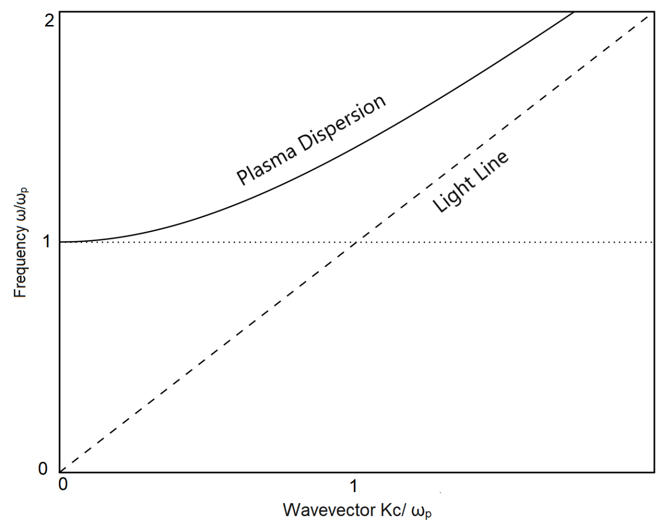

Figure 1.3: Dispersion relation for the free electron gas [1].

frequencies (i.e $\lambda < 550$nm), this model looses its validity. At higher frequencies, one need to take interband transitions into account, as there must be the probability of transition of electrons from the lower bands to conduction band. This phenomenon results in amendment of equation of motion (1.7) by addition of an extra force term given by

$$m\frac{\partial^2 \mathbf{r}}{\partial t^2} + m\gamma\frac{\partial\ \mathbf{r}}{\partial t} + \beta\mathbf{r} = -e\mathbf{E}(t) \tag{1.13}$$

and as a consequence, interband transition dielectric function takes the following new Lorentz-like form

$$\epsilon_{IB}(\omega) = 1 - \frac{\Omega_p^2}{(\omega^2 - \omega_0^2) + i\Gamma\omega} \tag{1.14}$$

where $\Omega_p = \sqrt{\frac{n^* e^2}{\epsilon_0 m^*}}$ with n^*, m^* are the density and effective mass of the bound electrons, $\omega_0 = \sqrt{\beta/m^*}$ is resonance frequency of bound electrons and Γ is the damping parameter for bound electrons.

1.3.3 Theory of surface plasmon polaritons

To investigate the physical properties of the propagating SPPs, one need to take into account the solutions to the Maxwell's equations with the relevent boundary conditions at interfaces. Starting from the general wave equation given by

$$\nabla^2\mathbf{E} - \frac{\epsilon}{c^2}\frac{\partial^2\mathbf{E}}{\partial t^2} = 0 \tag{1.15}$$

these propagating waves trapped at the metal/dielectric interface can be described in two steps. First, assuming the time dependent harmonic field $\mathbf{E}(\mathbf{r}, t) = \mathbf{E}(\mathbf{r})\exp^{-i\omega t}$ and inserting into equation (1.15) yields

$$\nabla^2\mathbf{E} + k_0^2\epsilon\mathbf{E} = 0 \tag{1.16}$$

the so called Helmholtz equation, where $k_0^2 = (\omega/c)^2$ is the wavevector of the propagating wave. In the next step, we define the propagation geometry shown by figure (1.4).

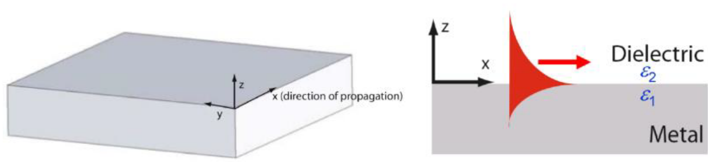

Figure 1.4: A schematic of propagation geometry and geometry of flat metal-dielctric interface for SPP propagation (xz view) [1].

Now, assuming the light source to be monochromatic with propagation direction x-axis in Cartesian coordinates, the propagating waves at the interface can be described by $\mathbf{E}(x, y, z) = \mathbf{E}(z)\exp^{i\beta x}$, with $\beta = k_x$ a propagation constant. Inserting this information into equation (1.16) takes form into

$$\frac{\partial^2\mathbf{E}(z)}{\partial z^2} + (k_0^2\epsilon - \beta^2)\mathbf{E} = 0 \tag{1.17}$$

with a similar equation holds for magnetic field $\mathbf{H}$. For each component of field $\mathbf{E}$ and $\mathbf{H}$, explicits expression can be found by taking advantage from both curl equation (1.3-1.4) and harmonic time dependence of fields ($\partial/\partial t = -i\omega$). Also along the propagation direction x ($\partial/\partial x = i\beta$) and for y-axis ($\partial/\partial y = 0$) due to no spatial movement in this direction, the following system of simplified equations can be found as

$$\frac{\partial E_y}{\partial z} = -i\omega\mu_0 H_x \tag{1.18a}$$

$$\frac{\partial E_x}{\partial z} - i\beta E_z = i\omega\mu_0 H_y \tag{1.18b}$$

$$i\beta E_y = i\omega\mu_0 H_z \tag{1.18c}$$

$$\frac{\partial H_y}{\partial z} = i\omega\epsilon\epsilon_0 E_x \tag{1.19a}$$

$$\frac{\partial H_x}{\partial z} - i\beta H_z = -i\omega\epsilon_0\epsilon E_y \tag{1.19b}$$

$$i\beta H_y = -i\omega\epsilon_0\epsilon E_z \tag{1.19c}$$

This set of equation can be further solved for two different polarization states TM (P) and TE (S), separately. For transverse magnetic (TM) case, only the field components E_x, E_z and H_y are nonzero and the set of equations (1.18-1.19) reduces to

$$E_x = -i\frac{1}{\omega\epsilon_0\epsilon}\frac{\partial H_y}{\partial z} \tag{1.20a}$$

$$E_z = -\frac{\beta}{\omega\epsilon_0\epsilon} H_y \tag{1.20b}$$

with the corresponding wave equation (Magnetic analogous to equation (1.17))

$$\frac{\partial^2 H_y}{\partial z^2} + (k_0^2\epsilon - \beta^2)H_y = 0 \tag{1.20c}$$

Whereas, for transverse electric (TE) case, only the field components H_x, H_z and E_y are nonzero and the set of equations (1.18-1.19) reduces to

$$H_x = i\frac{1}{\omega\mu_0}\frac{\partial E_y}{\partial z} \tag{1.21a}$$

$$H_z = \frac{\beta}{\omega\mu_0} E_y \tag{1.21b}$$

with the corresponding wave equation (equation (1.17))

$$\frac{\partial^2 E_y}{\partial z^2} + (k_0^2\epsilon - \beta^2)E_y = 0 \tag{1.21c}$$

Figure (1.4) shows a simple geometry for SPP propagation with a single interface between metal with dielectric function $\epsilon_1(\omega)$ $(z < 0)$ and dielectric with a positive constant ϵ_2 $(z > 0)$. Finally, we are in a condition to just apply the boundary conditions to fully describe SPPs for both states.

Let's first look up at the TM mode by Solving the system of equation (1.20) on the both sides of interface. Continuity of the field components (H_y) and $(\epsilon_i E_z)$ at the boundary (z=0) require $A_1 = A_2$ with

$$\frac{k_2}{k_1} = -\frac{\epsilon_2}{\epsilon_1} \tag{1.22}$$

and solving wave equation (1.20c) for H_y yields the propagation constants

$$k_1^2 = \beta^2 - k_0^2\epsilon_1 \tag{1.23a}$$

$$k_2^2 = \beta^2 - k_0^2\epsilon_2 \tag{1.23b}$$

Combining equations (1.22) and (1.23) finally results in the dispersion relation of SPP as

$$\begin{aligned} \beta &= k_0\sqrt{\frac{\epsilon_1.\epsilon_2}{\epsilon_1+\epsilon_2}} \\ k_{spp} &= \frac{\omega}{c}\sqrt{\frac{\epsilon_m.\epsilon_d}{\epsilon_m+\epsilon_d}} \end{aligned} \tag{1.24}$$

where ϵ_m and ϵ_d are the dielectric constants of metal and dielectric. ϵ_m could be real as well as complex and above mentioned dispersion relation holds for both cases. This constant is an important parameter to describe this phenomenon and connected with the refractive indices (n's) of the materials via relation $n = \sqrt{\epsilon}$.

Now, for TE surface modes, set of equations (1.21) solved for both sides across the interface. Continuity of field components E_y and H_x at the boundary leads to the condition

$$\begin{aligned} A_1(k_1+k_2) &= 0 \\ A_1 &= A_2 \end{aligned} \tag{1.25}$$

For the confinement to surface, it requires $\mathrm{Re}[k_1] > 0$, $\mathrm{Re}[k_2] > 0$ which can be only fulfilled when $A_1 = A_2 = 0$. As a consequence there are no SPP excitations for this mode of polarization and we can say SPP exist just for TM mode of polarization.

To know more about SPP properties, we can continue the discussion from equation (1.24). By inserting dielectric function of free electrons equation (1.9) in (1.24) yields the characteristic surface plasmon frequency given by

$$\omega_{sp} = \sqrt{\frac{\omega_p}{1 + \epsilon_m}} \tag{1.26}$$

At this frequency, propagation constant $\beta \rightarrow \infty$ resulting in the group velocity $v_g \rightarrow 0$ and Re$[\epsilon_m]$ = - ϵ_d ($\epsilon_d > 0$). The dispersion curve in figure (1.5) describes the relationship between different frequency regimes.

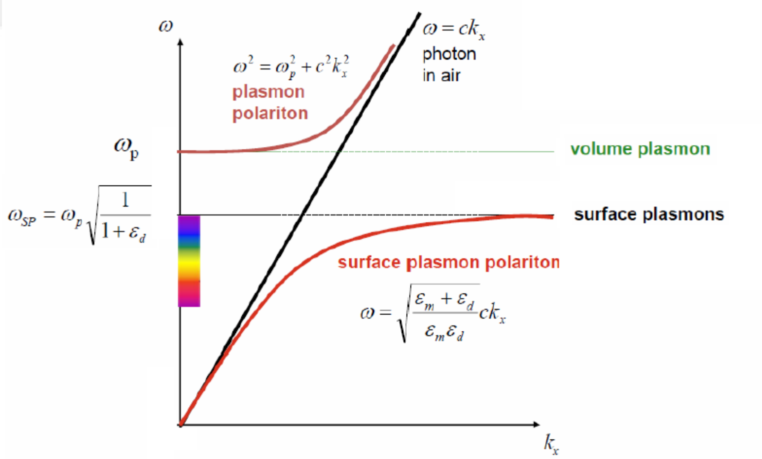

Figure 1.5: Dispersion curve of SPP on single metal-dielectric interface [26].

In the regime $\omega < \omega_p$, ϵ_m is real but negative and the dispersion curve for SPPs lies right to the light line. This suggest that for the same frequency ω, the wavevector of the SPP propagating along the surface is greater than the wavevector of light in air. With an increase in the frequency, SPP's dispersion curve shows a deviation from the light line and reaches an asymptotic frequency line, so called Surface plasmon frequency, ω_{sp}. For $\omega > \omega_p$, ϵ_m is real and positive. The wave propagates in the medium without any decay due to its positive wavenumber as given by Drude's Model.

1.3.4 Excitation of surface plasmon polaritons

Surface plasmon polariton can not be excited directly upon illumination of electromagnetic radiation due to large mismatch between their wavevector and photon's wavevector. To cope with this fact, many configurations have been developed to excite SPP e.g. prism coupling, grating coupling, usage of highly focused optical beams etc. Here, only a short description of grating coupling is given in an approach to this project.

In this technique, a periodic array of holes is patterned on the metallic surface with a lattice constant p to provides an additional momentum to overcome the mismatch in the wavevector between $k_{||}$ and β. For a simple one dimensional grating of grooves as shown in figure 1.6, phase can match only under the following condition

with $g = \frac{2\pi}{p}$ is the grating's reciprocal vector and $\nu = \{1, 2, 3, ...\}$ is the grating order. These SPP excitations usually appear as dips (*minima*) in the reflection spectrum of the light.

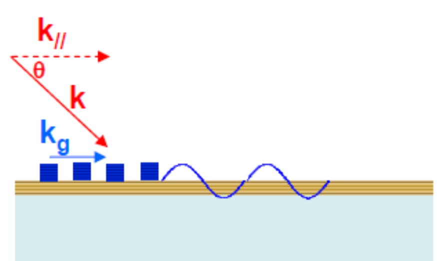

Figure 1.6: A schematic diagram of phase matching of light to SPPs using grating coupling technique [1].

1.4 Metamaterials

Metamaterial is a class of novel artificial materials having extraordinary characteristics lacking in naturally existing materials. This emerging field of metamaterial opened many doors for the researcher to focus on the electromagnetic properties of a vast variety of novel materials by tailoring their effective electromagnetic response. A metamaterial is usually composed of well organized periodic array of structures with a size much smaller as compared to their excitation or working wavelength. Electromagnetic properties of these materials are mainly described by permittivity and permeability, which can be tuned with a great precision in different ways to control the impinging electromagnetic waves [27, 28, 29]. Electromagnetic Cloaking, Imaging technologies, Energy harvesting , perfect absorbers are among some of the applications where this precise control of EM waves is demonstrated successfully. There are different kinds of metamaterials, among which Left handed materials with a negative refractive index have caught a special attention of the researchers for its remarkable novel class of applications e.g. invisibility cloaking, flat lens etc. High impedance surface is also a type of metamaterial, with thin metal-dielectric sheets exhibiting unique desirable properties by controlling their geometrical parameters [30]. An important phenomenon, Perfect Absorption, occurs when effective surface impedance ($Z_{eff} = \sqrt{\frac{\mu_{eff}}{\epsilon_{eff}}}$) of such a surface gets similar to the free space impedance (Z_{eff} = 1) at some certain frequency. These metamaterials are termed as Perfect Absorbers and are well studied over a range of electromagnetic spectrum from radio to optical frequencies [31].

1.5 Plasmonic Metamaterial Perfect Absorbers

Metamaterial electromagnetic absorbers have been frequently investigated aiming to achieve maximum absorbance, tunability of absorbance wavelength and operational modes by controlling geometrical parameters of the device and finding new ways for simpler fabrication. In such absorbers, reflection and transmitted powers are minimized to get high absorbance and have many applications like photo-detectors, photovoltaics, wireless communication and sensors. Extraordinary absorption properties of such a plasmonic absorber comes from intrinsic losses induced by excitation of plasmonic resonances in these special materials. These excitation originates from the collective oscillations of electrons by interaction of incident electromagnetic light with well organized nanostructures or metallic nanoparticles. By Properly designing and carefully controlling various geometrical parameters, these looses can be enhanced to achieve maximum absorbance via these excitations. Also excitations of different resonance modes consequently produce critical losses in such nanostructures, thus allowing to reach the perfect absorption.

Up to date, plenty of PMA have been reported theoretically as well as experimentally with its potential applications in the electromagnetic regime, spanning Radio frequency, Microwaves, Infrared and visible [22, 32, 33, 34, 35, 36, 37, 38]. Especially, in visible and infrared regime, these absorbers have a wide range of promising applications, which includes EM cloaking [39], optical switches [40], Thermal IR sensors [41], refractive index sensors [32], gas sensing [42], surface-enhanced spectroscopy etc [17, 18]. Furthermore, these metamaterial absorbers are categorized on the basis of absorption bandwidth into broadband and narrow-multiband absorbers.

1.5.1 Broadband PA

In literature, broadband perfect absorber are studied more extensively due to its large absorption bandwidth which makes them superior to utilize for energy harvesting, thermal emitters, thermophotovoltaics and security applications [43, 44, 45]. These PA actaully takes adavantage from high optical losses of the material used and excitation of several closely spaced plasmonic resonances to produce a large absorption bandwidth, and are studied over a range of EM spectrum [37, 38, 46]. For example in 2016, Fei Ding et al. [34] proposed a MIM based PA in the near-infrared region, where a thin sheet of SiO_2 is placed between a thick bottom gold layer and top periodic layer of nanodisks made up of Ti. High optical looses of Ti lead to absorption efficiency exceeding 90% over a broad spectral range from 900-1825 nm as shown in Fig. 1.7.

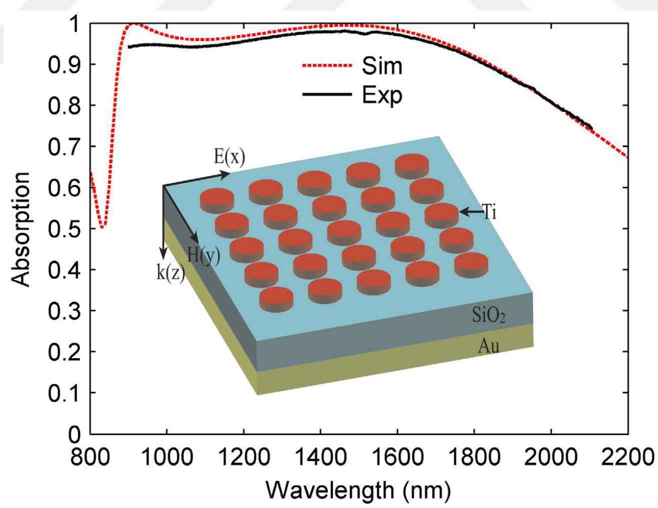

Figure 1.7: Broadband PA: Absorption spectra and design of a broadband PA in near-infrared region [34].

Similarly, in the visible to near-infrared region Lei et al. [47] proposed an absorber composed of a periodic array of titanium-silica (Ti-SiO_2) cubes sitting on a thick bottom film of aluminum. Their proposed PA came up with an average absorption efficiency around 97% spanning a large bandwidth from 354 nm to 1066 nm shown by Fig. 2.8.

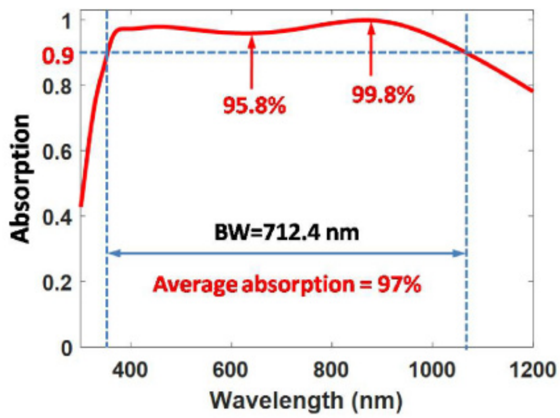

Figure 1.8: Ultra broadband PA: Absorption spectra of a broadband PA in visible to near-infrared region yieliding an average absorption efficiency of 97% with a high bandwidth of around 712 nm [47].

1.5.2 Narrowband PA

In contrast to broadband absorbers, for spectroscopic [48, 49] and sensing applications [50, 51], narrowband PA are preferred. Recently, scientists have also shown their interest in designing narrowband PA and plenty of efforts have been made so far to design ultra narrow-band plasmonic nanostructures to improve the quality-factor of resonance peaks despite many difficulties due to ohmic and radiative losses in the material [32, 51, 52, 53, 54]. Few years back in 2014, Meng et al. numerically demonstrated a narrowband absorber with absorptivity touching 98% mark, with a bandwidth of just 0.4 nm (Fig. 1.9 (a)) [55]. In the same year, Li et al. proposed an all-metal nanostructure based narrowband absorber, by experimentally achieving nearly 90% absorptivity with peak width of 20 nm (Fig. 1.9 (b)). Both these absorbers are based on a periodic layer of patterned nanostructures sitting on a thick metallic sheet and Lattice resonance in these all-metal nanostructures based absorbers is responsible for the ultra-narrow bandwidth and is somehow not easy to satisfy due to limitations in designing the structure [56]. But, the most typically PAs are composed of a multilayer metal-insulator-metal platform, where middle dielectric layer plays a crucial role to achieve perfect absorption, and are discussed in detail below.

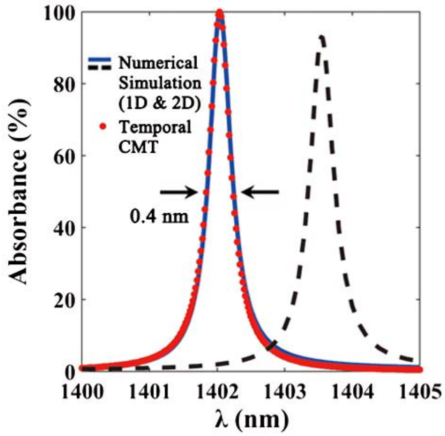

(a)

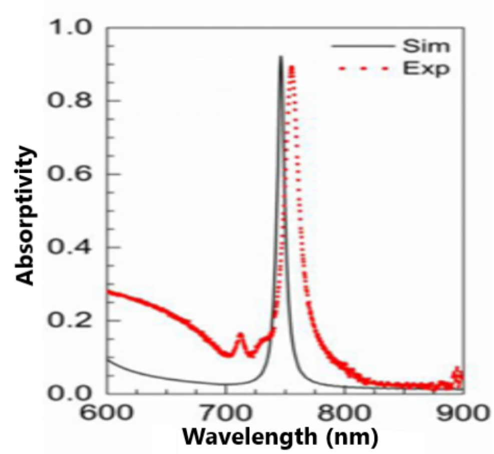

(b)

Figure 1.9: Absorption spectra of the narrowband absorbers based proposed by Meng et al. (a) and Li et al. (b).

1.5.3 Metal-Insulator-Metal Plasmonic PA

Recently, a particular interest have been developed in Metal-Insulator-Metal(MIM) based plasmonic metamaterials, and are investigated intensively due to near unity absorption and ultra-narrow bandwidth. Typically, these absorbers consist of a thin dielectric spacer sandwiched between a bottom metallic plate and a continuous [33] or patterned periodic metal absorber layer on the top [38, 52] as shown in Fig. 1.10. There is a possibility to choose the lattice structure such as square, triangle, hexagonal and honeycomb. Whereas, the top nanosized patterned metallic structures could be designed in different shapes such as square, rectangles, circles, bow-ties, cross-shaped, to name but a few. The shape of these patterns play an important role to define single or multiband resonance modes. Thickness of the bottom metal plate, placed a subwavelength gap from the well patterned top periodic metal layer, is set to be electromagnetically thick to minimize the transmitted power meanwhile sustaining the plasmonic resonance in the device. By illuminating such an absorber with electromagnetic radiation, absorption of incident light take place due to minimization of reflection around the resonant frequencies. Together with the thick ground metallic plate to minimize transmission and excitation of plasmonic resonances with the help of critical coupling and impedance matching phenomenons under certain conditions, lead to zero reflection ensuring perfect absorption.

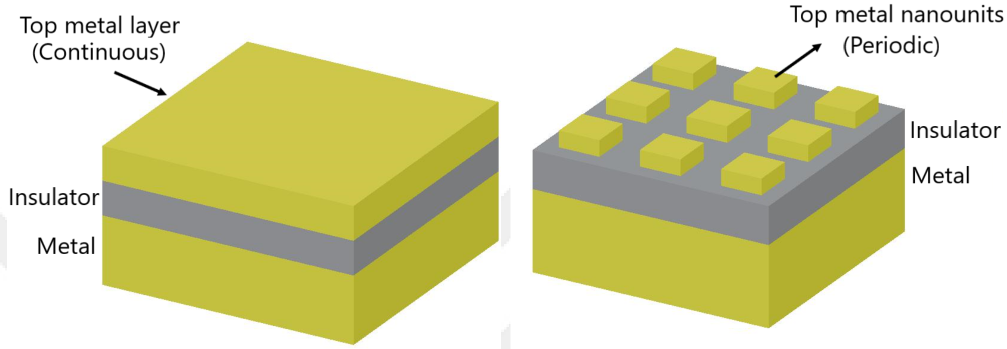

(a) (b)

Figure 1.10: A schematic view of MIM based plasmonic absorber with a continuous **(a)** and periodic patterned nanostructured **(b)** top metal layer.

In such kind of absorbers, the bottom and top layers are usually based on metals such as silver(Ag) [57], gold(Au) [48], aluminum(Al) [58]. Meanwhile, Graphene, highly doped silicon(Si), tungsten(W) and molybdenum(Mo) are also the candidates for above mentioned layers [59, 60, 61, 62]. The middle dielectric spacer could be either nitride or oxide e.g. silicon nitride(SiN) [58] , aluminum nitride(AlN) [62], silicon dioxide(SiO_2) [47], aluminum dioxide(Al_2O_3) [63]. Also, Magnesium fluoride(MgF_2) and calcium fluoride(CaF_2) can be used as dielectric spacer [48].

These narrowband PAs usually show up a single absorption peak upon excitation of a plasmonic resonance. For example, Liu et al. proposed a narrowband PA based on MIM configuration, where an Al_2O_3 spacer layer is placed between a bottom gold film and top periodic layer of cross-bar shaped nanoantennas, resulting in a single absorption peak as shown in Fig. 1.11(a) [63]. A similar kind of structure was proposed by Kai chen et al., where a sheet of MgF_2 is inserted between a bottom gold plate and top layer of periodic cross-bar resonators. By simply playing with the symmetry of top cross bars, multi-resonant behaviour was appeared in the reflection/absorption spectra of the device as shown in Fig. 1.11(b) [48].

Such kind of Multi-resonant PAs are very demanding especially in the Infrared region, where it can simultaneously detect and identify different biomolecules employing Surface enhanced infrared absorption (SEIRA) spectroscopy.

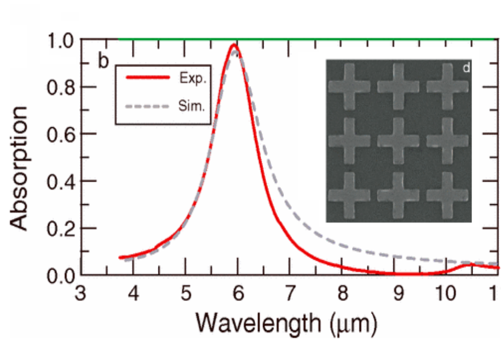

(a)

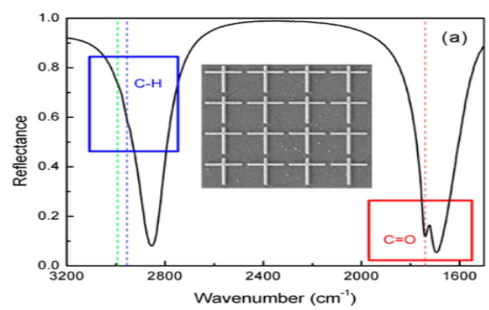

(b)

Figure 1.11: Absorption / Reflection spectra of uni-resonant (a) and multi-resonant (b) Metal-Insulator-Metal (periodic cross-bars) configuration based narrowband perfect absorbers [63, 48].

1.5.4 Physics behind Perfect absorption of MIM plasmonic MM absorber

Metamaterial perfect absorbers are of much importance in many fields of science and technology such as microbolometers, thermal imaging, sensitive detectors, photovoltaics solar cells, to name a few. The physics behind perfect absorption can be explained in term of system's impedance matching with the input (air / vacuum) impedance and critical coupling phenomenons [48, 64] in addition to the excitation of plasmonic resonances. Here, we have discussed the perfect absorption phenomenon in only MIM platform based absorbers. Let's assume that the incident energy can be just reflected, absorbed or transmitted from/ by the metasurface such that the sum of all these is unity ($\mathbf{R + T + A = 1}$). So, for such a system to achieve near unity absorption, the idea is to minimize the transmission and reflection of the system. To minimize the transmission of device is quite easy for which the bottom metallic plate in made enough thick (more than the skin depth of the metal) that it does not let any incident light to pass through it and plays a critical role to minimize the transmission ($\mathbf{T} =$

0). Then absorption of the system can be found from the reflection by (**A = 1 - R**). To minimize the reflection, the system is designed in such a way that upon incidence to EM radiations, plasmonic resonances are excited in the system at certain frequencies that leads to impedance matching and critical coupling when certain conditions are satisfied. So, all the incident energy is absorbed by the system and dissipated in the structure due to ohmic or dielectric losses of the system.

1.5.5 Sensing with MIM plasmonic absorbers

Plasmonic nanoparticles based multilayered MIM system has a great potential to serve as a sensing device due to its subwavelength scale spatial dimensions and sensitivity to any change in the surrounding environment. These characteristics make such a device to show up some promising applications in the fields of biomedical and material sciences. Plasmonic resonance based MIM metamaterial absorber are of particular interest for biosensing purposes due to favorable confinement of light in the visible/IR region of electromagnetic spectrum. Just like typical refractive index sensor, a resonance shift is monitored to sense any biomolecule placed on such a system. These absorbers actually take advantage from the excitation of plasmonic resonances. At these resonance wavelengths, the near fields strongly enhance around the metallic nanostructures and, thus boosting the interaction between incident electromagnetic radiation and the structures. These interactions are very sensitive to the surrounding environment, and any change in the ambiance cause a shift in the resonance peak which can be monitored to sense biochemicals etc. There are some certain parameters that quantifies the performance of such a sensor, which depends on several geometrical parameters and material properties.

Sensitivity and Figure of Merit(FOM) are two commonly used parameters to quantify plasmonic sensor's performance. As the resonance conditions for a plasmonic sensor strongly depends upon its surrounding's dielectric permittivity, a shift appears in the resonance wavelength as consequence of any environmental change. Sensitivity($\mathbf{S}$) is defined as change in the resonance wavelength (λ_{res}) per unit change in refractive index (n) of the surrounding medium and is given as

$$\mathbf{S} = \frac{\Delta\lambda_{res}}{\Delta n} \tag{1.28}$$

Sensitivity is a key parameter of such a sensor and plays a vital role in sensing measurements. However, sensitivity does not provide any information about the shape and sharpness of the resonance peaks. So, figure of merit (FOM) is the other useful parameter to analyze the sensor's performance which is defined as

$$\mathbf{FOM} = \frac{\mathbf{S}}{\mathbf{FWHM}} \tag{1.29}$$

where **FWHM** defines the full width at half maximum of the resonance peak. Also, there is another dimensionless parameter that is compared with the band-width of plasmonic resonance peak, called Quality factor($\mathbf{Q}_f$). It is defined as a ratio of resonance wavelength and FWHM of the resonance peak and strongly depends on the damping constant (γ) of the corresponding metal, given as

$$Q_f = \frac{\lambda_{res}}{FWHM} \tag{1.30}$$

Chapter 2

Design and Simulations

In this work, a narrow band Metal-Insulator-Metal plasmonic absorber is proposed with top metal layer as a patterned 2-D metallic circular nanodisks periodically spanned in the lateral directions as shown in Fig. 2.1. For the top and bottom metallic layers gold is used, whereas MgF_2 is considered for middle insulating layer. The whole MIM system sits on a transparent glass substrate. To calculate the far-field and other numerical analysis, proposed system is simulated by Finite difference time domain (FDTD) method using a commercial software Lumerical Inc.

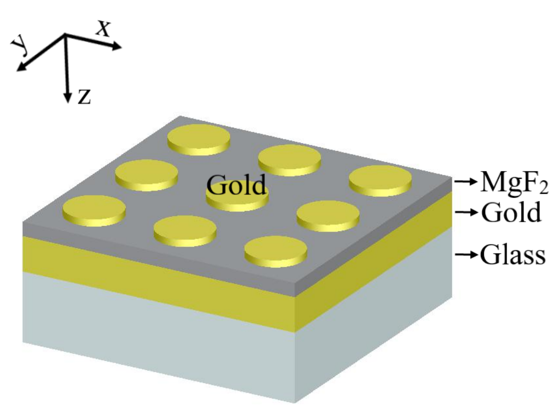

Figure 2.1: A schematic of the proposed MIM metamaterial absorber.

2.1 Finite difference time domain Solver

FDTD is a state of art method to solve Maxwell's equation in time and space for complex geometries. FDTD solver also provides frequency solutions to calculate a range of useful quantities such as transmission/reflection of light and Poynting vector by exploiting Fourier transforms. In contrast to finite element solvers which requires separate simulation for each frequency, it offers the user a broadband simulations over a frequency range in a single run . This solver is reliable and well suited to analyze the interaction of electromagnetic radiation with complicated structures at subwavelength scale.

2.1.1 Background Physics

FDTD solver solves any electromagnetic or photonic problem by solving Maxwell's curl equation given by

$$\frac{\partial \vec{H}}{\partial t} = -\frac{1}{\mu_0} \nabla \times \vec{D} \tag{2.1}$$

$$\frac{\partial \vec{D}}{\partial t} = \nabla \times \vec{H} \tag{2.2}$$

$$\vec{D}(\omega) = \epsilon_0 \epsilon_r(\omega) \vec{E} \tag{2.3}$$

where D, E and H are electric displacement, electric and magnetic fields, respectively. ϵ_0 is free space permittivity and $\epsilon_r(\omega)$ is complex relative dielectric constant given as $\epsilon_r(\omega) = n^2$, where n is refractive index of the material under consideration.

Maxwell's equations have total six field components given by E_x, E_y, E_z, H_x, H_y and H_z, in 3 dimensions. If an assumption is made that the structure is infinite in z-axis and the fields are independent of z, such that

$$\frac{\partial \vec{E}}{\partial z} = \frac{\partial \vec{H}}{\partial z} = 0 \tag{2.4}$$

$$\epsilon_r(x, y, z, \omega) = \epsilon_r(x, y, \omega) \tag{2.5}$$

then the Maxwell's equation get separated into two different sets of equations termed as transverse electric(TE) and transverse magnetic(TM). Both TE and TM are then solved in only x-y plane for the vector components

TE: E_x, E_y, H_z

TM: H_x, H_y, E_z

These equations are solved by FDTD solver on a discrete temporal and spatial grid and each component of electric and magnetic fields is solved on different location within a grid cell, so called Yee cell, shown by Fig. 2.2. After collecting the data calculated at various points inside a grid cell, it is interpolated at the origin of each grid point by default.

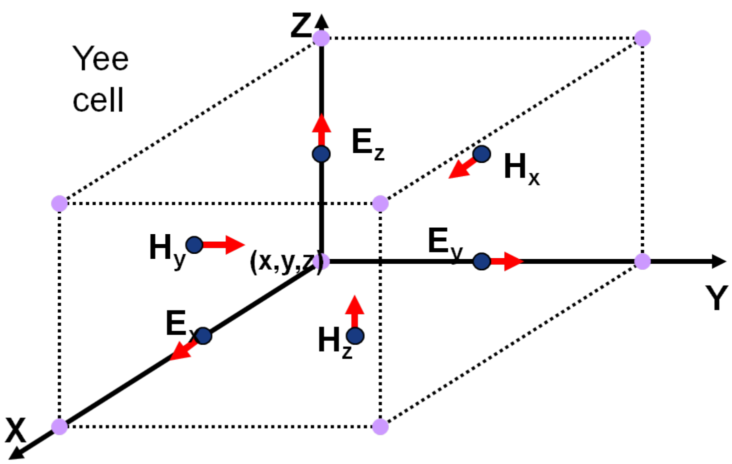

Figure 2.2: A Yee cell, showing how field components are solved at various points inside a grid cell [65].

2.2 Simulation Domain and Objects

To simulate a proposed structure, simulation domain defines many important simulation parameters such as simulation volume/area, Meshing, boundary conditions and simulation time. Also, there is range of simulation objects to solve a problem. Finite difference time domain (FDTD) is set to be the simulation domain, in which these simulations are carried out.

2.2.1 General and geometry settings

The general tab in the simulation region includes the information about the dimensions of simulation (2D/3D), maximum time allowed for simulation (simulation time), simulation temperature and background refractive index in which simulation is running. Whereas, geometrical parameters of the simulation region are defined by filling the information in the geometry tab.

2.2.2 Geometric and material parameters

After defining a simulation region, desired structure is inserted using structure tab available in the top main layout window. Then the dimensions of the structure can be set and material is chosen. Material is basically selected on the bases of its refractive index. There are two ways to choose a material; first is selecting the material from built-in available material and the second one is user defined by inserting the material's refractive index. In this work, gold, glass and silver are taken from built-in Palik data [66] while MgF_2 is defined by inserting its refractive index (**n=1.377**).

2.2.3 Mesh setting

FDTD solver solves Maxwell's equations using a Cartesian mesh and calculate fundamental simulation quantities e.g. electromagnetic field, material and geometrical properties at each mesh point. There are three types of meshes; auto non-uniform, custom non-uniform and uniform. Auto non-uniform is the default one which is controlled by Mesh accuracy parameter with a slid bar ranging from 1-8, with greater the number greater the accuracy of the simulation. For sub-cell scale accuracy, Mesh refinement parameter is used. Other settings include DT stability factor which defines the time step used for the simulation and minimum mesh step which gives the absolute minimum value for each interval for the whole region to be solved. For more accuracy, mesh override is also an option which can be used .

2.2.4 Boundary Condtions

Boundary conditions are one of the most important parameters to simulate the desired structure. There are six types of boundary conditions featured in this FDTD solver, and an appropriate boundary condition(BC) is required to impose to get the expected results. Below, these different types of BC's are discussed in detail.

Periodic boundary condition (PBC): Periodic boundary condition is used when both the structure and electromagnetic fields are periodic. This condition can be used in one, two or all three dimensions depending on the structure's periodicity. Periodic BC connects two ends of simulation domain and are applied to both negative and positive sides of any axis.

Perfectly matched layer (PML): Perfectly matched layer is a reflectionless boundary condition and has the ability to absorb the incident electromagnetic radiations. Infact, PML came from a basic concept of electromagnetism that, no reflection of waves takes place from the matched region in contrast to the unmatched region which reflect the waves back. For this boundary condition, usually default parameters are used except tuning the number of layers (typically

8 to 12), to prevent the incoming light to reflect back from the simulation domain.
Metal or perfect electric conductor (PEC): This boundary is applied to the surfaces which behave as a perfect electric conductor. Both, electric field component parallel to the metal boundary and the magnetic field component perpendicular to the metal boundary are zero. This makes it a perfectly reflecting boundary conditon and does not allow any power to escape the simulation region along that specific boundary.
Perfect magnetic conductor (PMC): PMC is magnetic equivalent of the metal PEC boundary condition. Here, magnetic field component parallel to the PMC boundary and the electric field component perpendicular to the PMC boundary are zero, yielding the condition for perfect reflection. But, it should be noted that PMC boundary condition is not experimentally realizable, whereas PEC can do the job.
Bloch boundary condition (BBC): This boundary condition is an extension to the periodic boundary condtion. BBC is used when both the structure and electromagnetic fields are periodic but there is a phase shift exists between each period. This condition is usually imposed when the periodic structure is excited obliquely.
Symmetric/Anti-Symmetric boundary condition: This boundary condition is used when the problem exhibits planes of symmetry, with both source and structure symmetric. Symmetric boundaries behave like a mirror for the electric field and anti-mirror for the magnetic field. Meanwhile, the reverse is true in case of anti-symmetric boundaries i.e. mirror for the magnetic field and anti-mirror for the electric field.

2.2.5 Sources

FDTD solver has a range of sources to excite the desired structure. These sources includes, point dipole source, Gaussian source, plane waves, total field scattered field (TFSF) source, mode source and customized import source.

2.2.6 Monitors

To record the calculated data, monitors are required to be placed at an appropriate position in the simulation region. There is a variety of these monitors in Luemrical's FDTD solver e.g. Index monitors, Movie monitors, frequency-domain field profile monitors, Frequency-domain power monitors, and Mode expansion monitors.

2.3 Simulating the proposed structure

In this thesis, simulation domain consists of a single unit cell of our periodic MIM structure, shown by Fig. 2.3. The rectangular unit cell has six faces and each face require an appropriate boundary condition. Here, we used two types of boundary conditions, periodic and PML as depicted in Fig. 2.3. Periodic boundary conditons are used on the surfaces of unit cell perpendicular to x and y axis as the proposed structure is periodic upto infinite extent in both x and y directions, whereas along z-axis PML are used. Whereas, to excite the proposed MIM structure an x-polarized plane waves source is injected along z-axis from top towards the structure. As the proposed absorber is designed to work in the visible-near-infrared region, the wavelength of the source is set to span from 400-1000 nm.

Frequency-domain power monitors are used to compute the reflection coefficient(R) and transmission coefficient(T) as electromagnetic radiation from the source get interacted with the designed structure. Then, the absorption of the system can be calculated easily using the formula **A=1-T-R**. If we consider the fact that, as the bottom layer is made optically thick resulting in almost zero transmission (T=0). Then, even there is no need of transmission monitor and absorption can be calculated by **A=1-R** by placing only reflection monitor above the source inside simulation region.

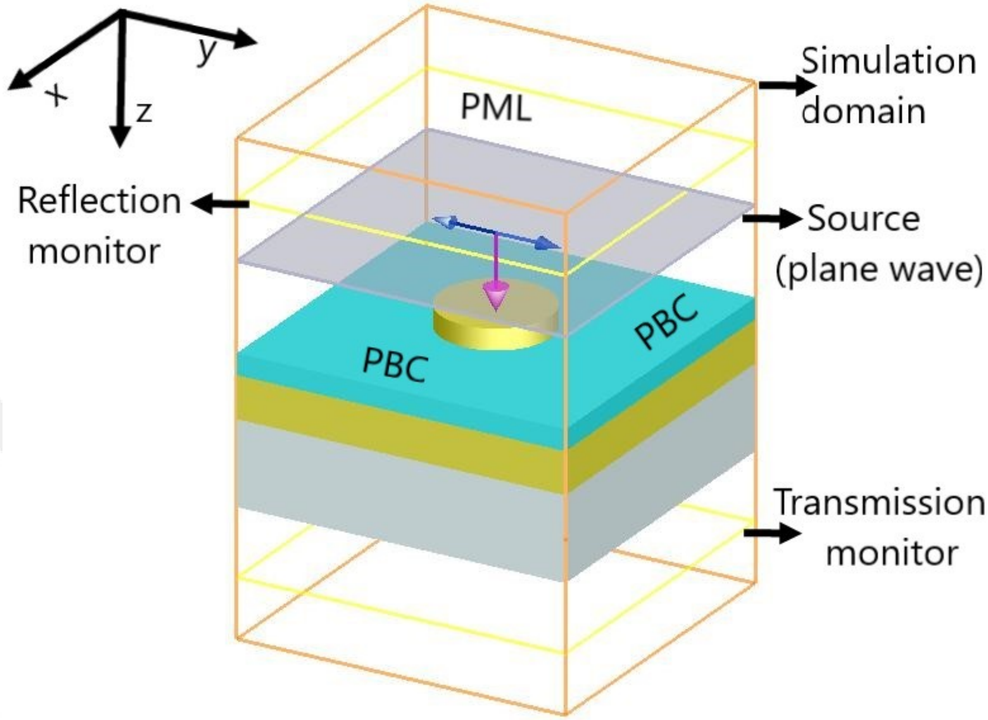

Figure 2.3: A Schematics of simulation domain employed to simulate the proposed MIM absorber with appropriate boundary conditions and simulation objects.

After defining the simulation domain with structure's geometry, sources and monitors, simulations are run simultaneous to get the proposed narrow band metamaterial absorber. Fig. 2.4 shows a unit cell of proposed MIM absorber which repeat itself with a period P in both x and y directions. It is based on an optically thick bottom gold layer of thickness $\mathbf{t}_B$ acting as a mirror to prevent any transmission in the system, middle dielectric $(\mathbf{MgF}_2)$ spacer of thickness $(\mathbf{t}_S)$ and top gold disks of thickness $(\mathbf{t}_T)$ with corresponding diameter $(\mathbf{D})$.

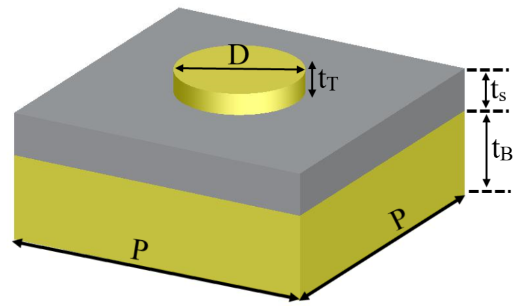

Figure 2.4: A schematic of unit cell of the proposed MIM absorber structure based on a bottom gold layer with thickness(t_B), t_S thick middle dielectric spacer, and top gold disk of diameter(D) with thickness(t_T).

Initially, structure with optimal parameters giving the maximum performance is demonstrated. Fig. 2.5 shows the reflection/ absorption spectra of the proposed MIM absorber with top periodic array of gold nanodisks with optimized geometrical features $\mathbf{t}_B = \mathbf{100\ nm}$, $\mathbf{t}_S = \mathbf{40\ nm}$, $\mathbf{t}_T = \mathbf{40\ nm}$, $\mathbf{D} = \mathbf{180\ nm}$ and periodicity $\mathbf{P}_x = \mathbf{P}_y = \mathbf{P} = \mathbf{600\ nm}$. Using Lumerical FDTD solver, reflection coefficient is computed by exciting the structure with a TM polarized plane wave source and then the absorption is calculated from the formula **A=1-R** as shown in Fig. 2.5. In the Reflection spectra, two dips with reflection reaching to zero appeared around 653nm (visible region) and 865nm (Near IR region) leading to two peaks with near unity absorption in the absorption spectra.

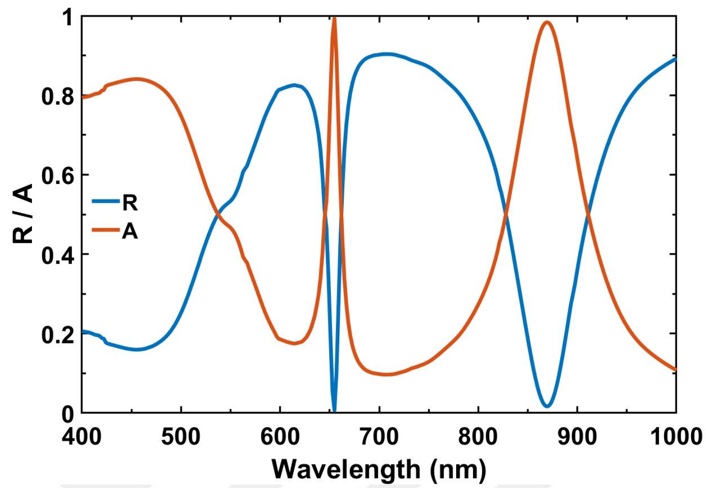

Figure 2.5: Simulated Reflection and Absorption spectrum of the system under study for optimized structural parameters, yielding a dual band spectra achieving near unity absorption with FWHM of 15nm and 80nm, respectively.

2.3.1 Physical origin of Reflection dips

The two dips appearing in the reflection spectra of the designed PA structure comes from the combination of LSP and SPP resonances as shown in Fig.2.6. The first resonant peak is sharper with a Full width at half maximum (FWHM) around 15nm, whereas second resonance peak has wider bandwidth with FWHM $\sim$ 80 nm. The first resonance around 653 nm corresponds to the (m,n) = (1,0) SPP mode at the spacer / gold film interface , where (m,n) is the grating orders of the reciprocal lattice vector G = (2π / P) $\sqrt{m^2+n^2}$ provided by the lattice with pitch constant P. Excitation wavelength of such a resonance depends strongly on the pitch constant of top periodic layer of gold nanoantennas, refractive indices of the corresponding metal (gold here) and surrounding material. Meanwhile, the peak appearing in the NIR region corresponds to the LSP resonance within top gold nanodisks particles and the corresponding resonant frequency is determined by the geometry (size, shape) of top resonating nanounit as well as the surrounding material's dielectric constant.

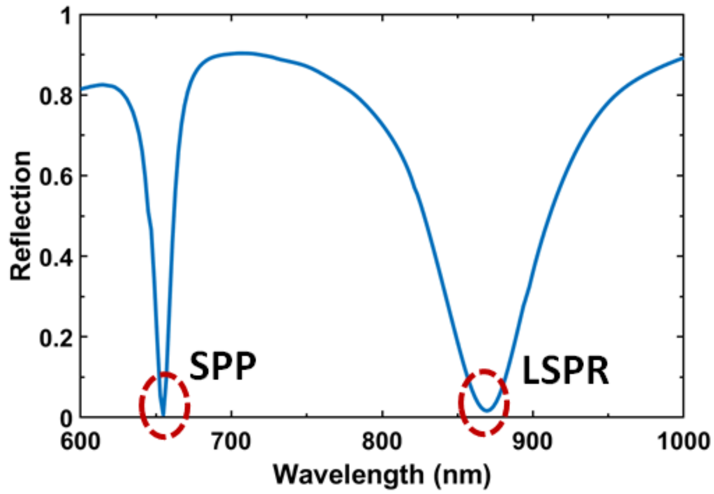

Figure 2.6: Simulation reflection spectra of the PA where the physical origin of reflection dips are shown to be the excitation of SPP and LSPR resonances at certain wavelengths.

2.3.2 Structural Parametric Effect

In order to better understand and investigate the effect of structural parameters (e.g. periodicity, dielectric spacer thickness, top nanodisks thickness and diameter) on the absorption and resonant characteristics of the proposed MIM absorber, many FDTD simulations are performed. Now, the effect of sweeping these parameters is discussed one by one as following.

2.3.2.1 The impact of periodicity

Periodicity is among the main and most significant factors, which plays a critical role to determine the position of resonance peaks. Many simulation are run with slight changes around our optimal periodicity P=600 nm. During simulations, other geometrical parameters **t_B=100 nm**, **t_S=40 nm**, **t_T=40 nm** and **D=180 nm** are fixed. Fig. 2.7 shows the impact of periodicity on the system's resonance peaks and absorption characteristics. As the periodicity swiped from 500 to 700 with an increment of 50nm, huge red shift in the first resonant peak is observed with a slight change in the peak amplitudes as well as the respective bandwidths. In Fig. 2.7(a), yellow diamonds shows that the first resonance wavelength linearly follows the periodicity . Whereas, the other broadband peak at longer wavelength is not much affected by this factor as there is just a slight shift in the resonance wavelength. In consequence to a huge red shift in the peak appearing at shorter wavelength, as the period swept from 500 to 700nm inter-peak distance decreases upto 20%. Fig. 2.7(b) plotted the absorption resonance peak amplitude as a function of the lattice constant (P) of the nanodisks based MIM absorber. Even for small values of lattice constant (P), amplitude of resonance peaks touches almost 90% and reaches upto unity absorption in the region P= 600-700 nm. Both the peaks have slightly different amplitudes for some values of period, however a remarkable difference in the bandwidths of two resonant peaks can be seen. Discrete sharp bands for the first resonance are observed, while wider bands for the second mode which are overlapping with the bands for different values of P appears as depicted in Fig. 2.7(a). At-last, we can say that periodicity defines the position and bandwidth of the first narrow-band resonance peak as it appears from the excitation of propagating plasmon resonance at the bottom gold film / dielectric spacer interface and the resonant wavelength of such a resonance is proportional to the lattice constant of the system under study. However, no significant changes can be seen in the absorption characteristics of the relatively broadband peak showing up at lower frequency.

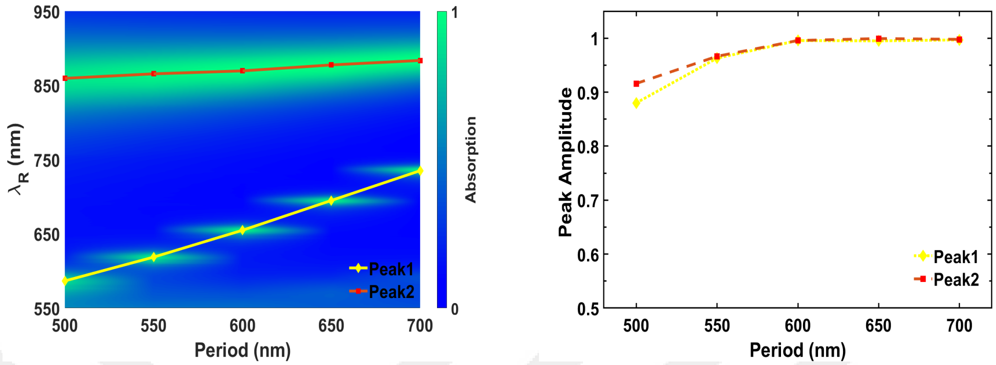

Figure 2.7: (**a**) Absorption (color scale) and resonant wavelength (first peak : yellow diamond, second peak: red square) of the system under study, (**b**) absorption efficiency at resonance wavelengths; as a function of the array pitch constant P.

2.3.2.2 The impact of dielectric spacer thickness

Middle insulator(MgF_2) sheet also plays a key role to absorb the impinging electromagnetic radiations and there is a need to exactly tune the thickness of this middle spacer layer to achieve an ideal absorber with narrow-band and highly absorptive features. To observe the role of the dielectric spacer thickness, simulation are performed by sweeping the t_M from 20 - 70 nm with a step of 10 nm. During the simulations, other geometrical parameters **t_B=100 nm**, **t_T=40 nm**, **D=180 nm** and **P=600 nm** are kept fixed. In Fig. 2.8(a), absorption and resonant wavelength is plotted as a function of dielectric spacer thickness. By increasing the t_S, a small red shift in the first resonance peak (Yellow dotted line in the figure) and a blue shift in the second excitation peak (Red dashed line in the figure) appeared in the absorption spectra of the system, consequently reducing the inter-peak distance.

Fig. 2.8(b) plotted amplitude of the absorption resonance peaks of the proposed MIM absorber with a sweep in the thickness of middle insulator. There exists a certain value of thickness (critical value) which yields maximum absorption. It can be seen that in the beginning, absorption efficiency of both resonant peaks increased by making an increment in the spacer thickness, but after a certain point (critical / optimum thickness) it again starts falling towards lower values of absorption amplitude. As our goal is to achieve maximum absorption by tuning various geometrical parameters of the system, peak amplitudes for both excited peaks converges around our optimal value of dielectric thickness (t_S=40 nm) as witnessed in Fig. 2.8(b). It can be explained by the fact that as the dielectric thickness starts increasing, plasmon coupling between the bottom film and top nanodisk strengthens and at the critical thickness these plasmons have strong coupling which gives the maximum absorption. A further increase in the thickness weaken the coupling and thus reducing the absorption efficiency of the system.

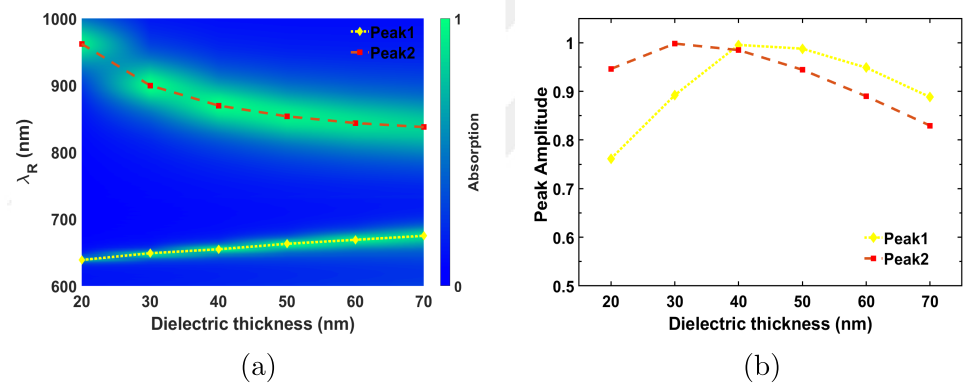

Figure 2.8: (**a**) Absorption (color scale) and Resonant wavelength (Peak1 : Yellow diamond , Peak2 : Red square), (**b**) Absorption resonance peak amplitude; as a function of dielectric spacer thickness.

2.3.2.3 The impact of top gold nanodisks thickness and diameter

To explore the impact of top metal periodic nanoresonators (gold nanodisks) in the absorption response of MIM absorber, a sweep is applied for thickness and radius of the top nanodisks. Before optimizing the parameters like radius and thickness of the top nanodisks, a case is mentioned without top plasmonic layer for MIM structure. In such a case, system behaves like a dielectric spacer coated mirror and reflects most of the incident light without any efficient absorption. As evident from Fig. 2.9, when there is no top resonant unit most of the light is reflected and resonant behavior is not observed (blue line in Fig.2.8). But addition of the top nanodisks (D = 130 nm) even with a small thickness (t_T = 10 nm) in the system, yields a resonant behavior in the absorption spectra as shown by green line in Fig. 2.9. This resonant behavior comes from the excitation of plasmonic resonances due to collective oscillation of electron in along the metal / dielectric layers. By controlling the coupling of incident electromagnetic radiation with these excitations, such a device can harness the incident light in the desired designed frequency range.

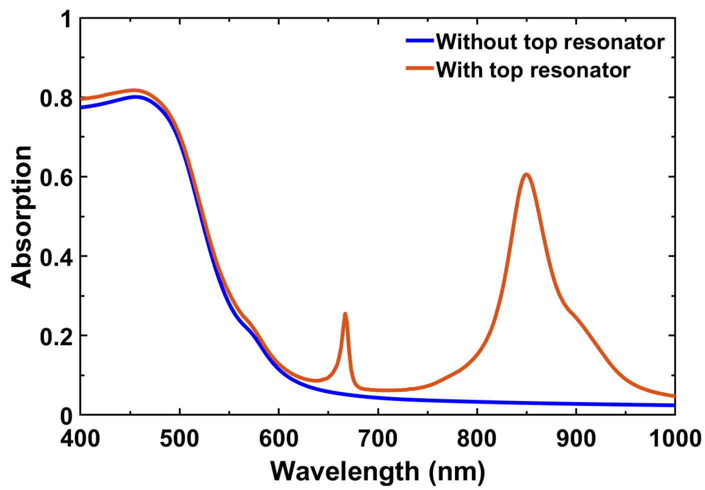

Figure 2.9: Absorption as a function of incident light wavelength, with and without top metal resonant layer.

Thickness of this top nanoresonator plays a crucial role in the absorption strength and bandwidths of the resonant modes. If these top units are made too thick, scattering from these top thick metallic particles enhances and they will not allow any light to pass through the system which results in the dominance of this top plasmonic layer's response over sandwiched dielectric cavity mode's response. In contrast, making these units too thin, weakens the strength of plasmonic coupling and there is no efficient absorption can be observed. So, we also need to optimize this parameter to achieve maximum performance of our system. For this purpose, thickness t_T is swiped from 20-70 nm with a step of 10 nm by keeping other parameter constant as $\mathbf{t}_B$ **= 100 nm**, $\mathbf{t}_S$ **= 40 nm**, **P = 600 nm** and **D = 180 nm**.

As illustrated in Fig. 2.10(a), an increase in the thickness shifts the second resonant peak towards lower wavelengths (red dashed line) while the first peak is not much affected by this factor. As discussed earlier, thickness also effects the absorption strength, Fig. 2.10(b) plotted the efficiency of absorption resonance peaks for different values of t_T. As moving towards thicker top plasmonic layer, the first peak becomes more stronger reaching up-to maximum value in the range 40-50nm (yellow dotted line), whereas the second peak looses its strength as we move further towards higher thicknesses(red dashed line) due to scattering. From Fig. 2.10(b), it can be seen that the absorption strength of both the peaks overlaps with near unity peak amplitude around our optimal value for thickness (critical thickness) $\mathbf{t}_T \approx$ **40 nm**.

Finally, the last parameter for investigation is the radius/diameter of top nanodisk resonator. To maximize the proposed system's performance, both $\mathbf{t}_S$ and $\mathbf{t}_T$ are fixed at **40nm** and a sweep is conducted on diameter (**D**) of the top resonating nanodisks array for five different values of D within **120 - 200 nm** with a step of **20 nm**. Absorption maps for different radii have been depicted in Fig. 2.11. Increment of radii does not put any remarkable effects one first resonant peak (Yellow diamonds) while a huge red shift in the spectral locations of second resonant mode is observed (red dashed line) owing the localized nature of the this resonance which depends on shape, size and geometry of the top units. Besides these shifts, as the radii increase the strength of absorption resonance

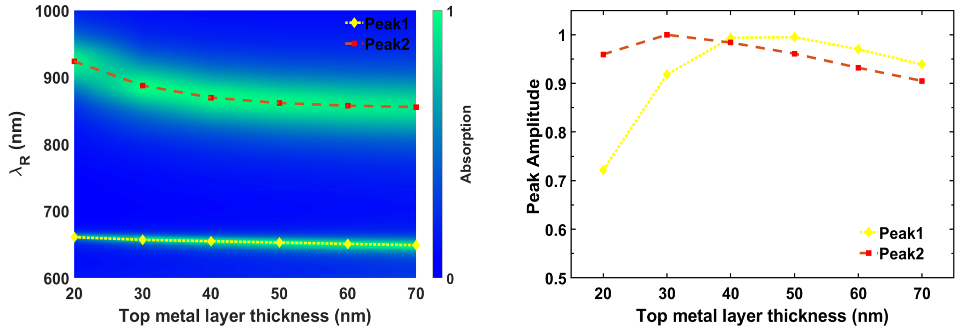

(a) (b)

Figure 2.10: Absorption and resonant wavelength as a function of top gold nanodisks thickness(t_T) (**a**), Absorption Resonance Peak amplitude for different values of top gold nanodisks thickness (**b**).

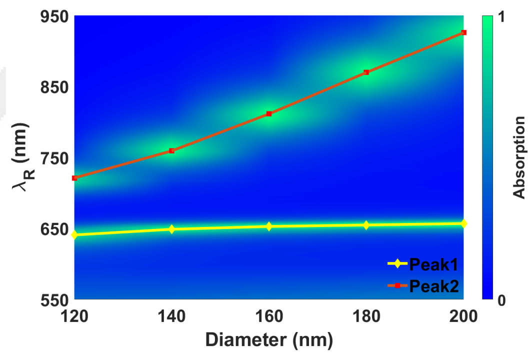

Figure 2.11: Absorption and resonant wavelength as a function of diameter D of the top nanodisk resonator array.

peaks fluctuates and is maximum for our optimum diameter (**D = 180 nm**) in this work.

2.3.3 Polarization dependence

To investigate the polarization dependence of the proposed MIM absorber, simulations are run by injecting the source on the structure with three different polarizations angles 0^0(x-pol), 45^0 and 90^0(y-pol). Fig. 2.12 plotted the absorption spectra for the above mentioned polarizations of the proposed system with optimized structural parameters. As from figure it is clear that there is no change in the absorption characteristics of the absorber for different polarizations, so the proposed system is polarization insensitive. The circular symmetry of the top metallic resonating layer is responsible for this characteristics of the proposed system, as it corresponds similarly to different polarized states of the incident light.

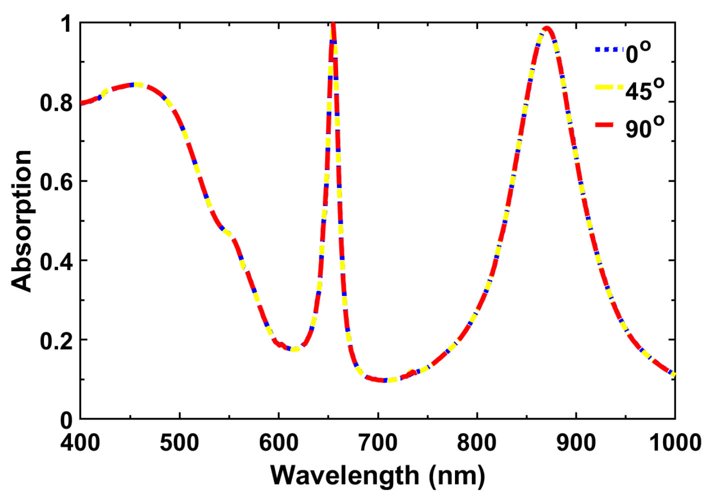

Figure 2.12: Absorption spectra of the MIM perfect absorber as a function of wavelength for different polarization angles.

2.3.4 Material dependence

In this section, we investigated the effect of materials which can be used for the composition of designed metamaterial absorber, discussed below.

2.3.4.1 Impact of material for bottom and top periodic layer

As, our structure is Metal-Insulator-Metal based platform, for the top and bottom layer, a metal usually gold or silver is preferred. So, we performed Numerical simulations to examine the behavior of absorption Spectra's dependence on the chosen metal, gold, silver and Aluminum. These simulations are run for the designed absorber with the optimum parameters i.e. $\mathbf{t}_B$ **= 100 nm**, $\mathbf{t}_S$ **= 40 nm**, $\mathbf{t}_T$ **= 40 nm**, **D = 180 nm** and periodicity **P = 600 nm**, by just changing the most top and bottom material. The optical data for the Silver and Aluminum is taken from the built-in Palik data. Fig. 2.13 shows the simulated reflection / transmission / absorption spectra for all three metals i.e. Gold (a), Silver (b) and Aluminum (c). When we switched from Gold to Silver, SPP (1,0) and LSP modes appeared around the same frequencies as in the Gold case however with somehow less absorption efficiency comparatively, which can be tuned by slightly changing the geometrical parameters of the system. However, interesting thing in the case is the addition of two more resonance peaks which are observed at the shorter wavelengths around 516 nm and 442 nm, which corresponds to the higher order SPP modes along the gold film. Similarly, for the Aluminum based top periodic and bottom continuous metallic layers based system, a higher order SPP mode is excited around 470 nm. Meanwhile, it can be observed from Fig. 2.13 (d) that, both LSP and PSP modes for the Gold and Silver particles appear around the same frequencies but for the Aluminum case both the modes showed a blue shift and are excited closed to each other owing to the strong coupling of plasmons. Here, we used the same parameters as used for the Gold based absorber, we can tune the other structures as well to get perfect absorption.

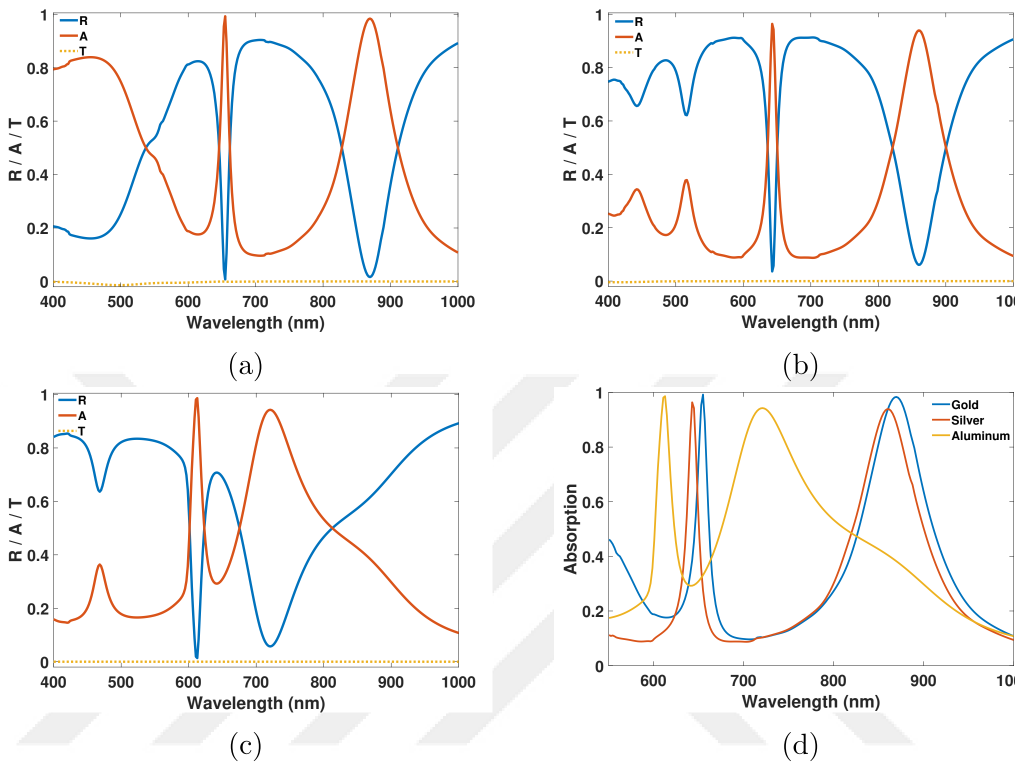

Figure 2.13: The simulated Reflection (R), Transmission (T) and Absorption (A) spectra for the Top / Bottom metal layers made up of Gold (a), Silver (b), Aluminum (c). A comparison of the absorption characteristics of the proposed absorber for the all three metals used for Top / bottom metallic layers.

2.3.4.2 Impact of material for middle dielectric spacer

We also investigated the absorption and resonant behavior dependence on the dielectric spacer material, for which we run various simulations by changing the refractive index values of the middle dielectric spacer layer n_S. Fig. 2.14 (a) shows the evolution of absorption as a function of n_S for the proposed absorber with optimum parameters. It can be seen from the figure that even for a small value of refractive index n_S , absorption is exceeding 90% and we can realize the perfect absorbance with both modes for n_S = 1.38 (MgF_2), 1.46 (SiO_2) and 1.50. In comparison to the absorption efficiency, resonant wavelength seems more sensitive to the dielectric refractive index as evident from the Fig. 2.14 (b). Resonant wavelength for both the modes depends linearly on the n_S in the studied range and can be fitted as $\lambda_1 = 84n_S + 540$ and $\lambda_2 = 393n_S + 331$, where λ_1, λ_2 are the resonant wavelengths for both the modes, respectively. As the refractive index of the gold in this regime is very linear, which leads to the linear dependence of resonance frequencies on n_S. We also noted that the tuning sensitivity of the mode 02 is much higher than the mode 01, which reaches around 400 nm.

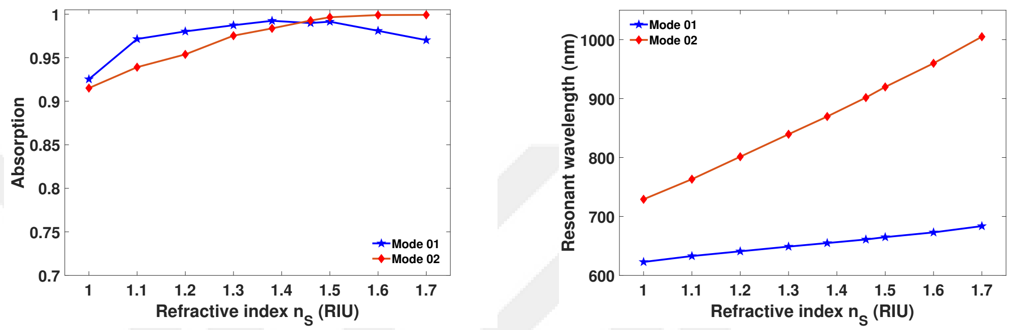

(a) (b)

Figure 2.14: Absorption (a) and Resonant wavelength (b) as a function of refractive index of the dielectric layer (n_S).

2.3.5 Shape dependence of top nanounit array

In this section, We investigated the effect of top resonator shape on the absorption efficiency and resonant frequency of the MIM absorber for six different shapes which are shown in Fig. 2.15. All other parameters of the system (i.e. t_B, t_S, t_T, P) are kept constant as in the above section, just the top resonating unit is changed with the geometrical parameters given in the table 2.1. Figure 2.16 (a) shows the absorption spectra for all the shapes with the parameters given in the table 2.1. It can be seen that the absorption efficiency of most of the systems is approximately same, and by just small changes in the device's parameters, the perfect absorption cab be achieved for those system's as well which yield somehow less absorption comparatively. Figure 2.16 (b) shows the resonant wavelength as a function of various shaped nanoparticles based top periodic metallic layer. We found that a change in the shape of top layer, only the second resonance showed a quick response by a change in the resonant frequency, meanwhile almost no notable response is given by the first resonance mode at lower wavelengths. This confirms our expectation that one of the factors which defines the resonance wavelength of LSP mode is the shape of top nanounits, but this factor does not play any significant role to determine PSP mode, as evident from Fig. 2.16 (b).

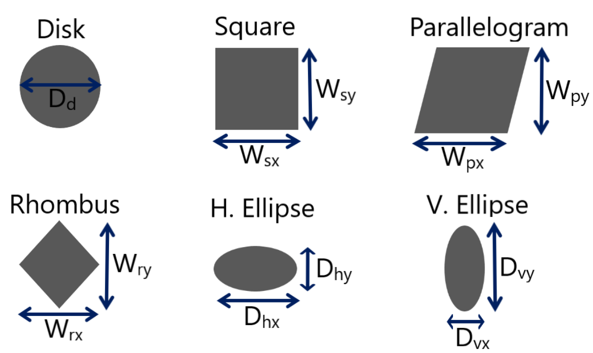

Figure 2.15: Six different shapes of the top metallic periodic array used to perform simulation to understand the behavior of MIM platform based structure.

Shapes	Geometrical parmeters (nm)
Circular Disk	$D_d = 180$
Square	$W_{sx} = W_{sy} = 180$
Parallelogram	$W_{px} = W_{py} = 180$
Rhombus	$W_{rx} = W_{ry} = 180$
Horizontal Ellipse	$D_{hx} = 180$; $D_{hy} = 120$
Vertical Ellipse	$D_{vx} = 120$; $D_{vy} = 180$

Table 2.1: Geometrical parameters corresponding to different shapes used for the top resonating metallic layer.

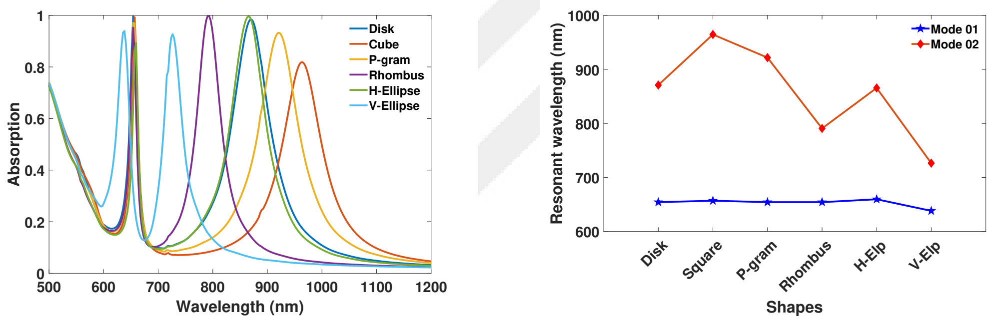

(a) (b)

Figure 2.16: Absorption (a) and Resonant wavelength (b) as a function of various shapes of top periodic layer of nanounits.

2.4 Impedance Analysis

Here, to explain the physical mechanism of the perfect absorption of the proposed MIM plasmonic absorber, we calculated impedance at the resonant frequencies. We performed the FDTD simulations to get S-parameters, which can be then used to retrieve the impedances. S-Parameters are actually the complex amplitude reflection and transmission coefficients of the system, and can be measured from the built-in S-Parameters analysis group in the Lumerical FDTD solutions. Fig. 2.17 shows a schematic explaining the principle to calculate these complex reflection / transmission coefficients. Only unit cell of the proposed metamaterial absorber is considered and illuminated by plane wave source from both the direction (inputs I_1 and I_2), then the output signal O_1 and O_2 are given by

$$\begin{pmatrix} I_1 \\ I_2 \end{pmatrix} = \begin{pmatrix} S_{11} & S_{12} \\ S_{21} & S_{22} \end{pmatrix} \begin{pmatrix} O_1 \\ O_2 \end{pmatrix} \tag{2.6}$$

where, S_{11}, S_{22} are the complex reflection, and S_{21}, S_{12} are the complex transmission coefficients for the I_1 and I_2 incidence signals, respectively. These parameters can be defined from incident (E_i) and reflected (E_r) / transmitted (r_t) electric fields as $S_{11} = (E_r) / (E_i)$ and $S_{21} = (E_t) / (E_i)$ for I_1 incident plane wave and vice versa for the I_2 incidence.

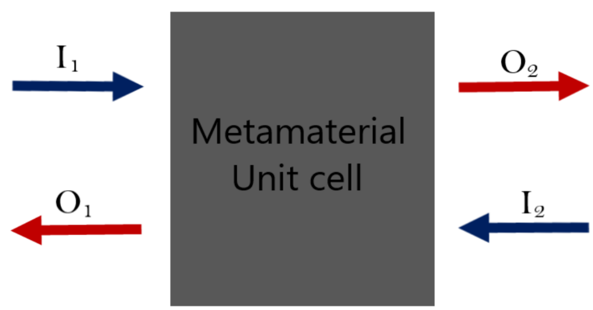

Figure 2.17: A schematics of S-parameter calculation principle for a metamaterial from FDTD simulations.

Once, we have the S-parameters , we can retrieve the impedance (Z) and other effective properties of the device easily [67]. But, the calculations of these parameters strongly depends on the homogeneity of system and falls into two different categories discussed below.

2.4.1 Case 1 : Symmetric behavior of the device

When the device under study behaves similarly for the forward / backward propagating sources, i.e. $S_{11} = S_{22}$ and $S_{21} = S_{12}$, we can take advantage from the symmetry of system and the device is only illuminated from either direction. Let's consider, the system is excited from forward direction with incidence source signal I_1, then from S-parameters analysis we will get S_{11} (reflection) and S_{21}

(transmission). Then the impedance and other effective properties (i.e. refractive index, permittivity and permeability) of the device can be found from the following equations

$$Z_{eff} = \sqrt{\frac{(1+S_{11})^2 - S_{21}^2}{(1-S_{11})^2 - S_{21}^2}} \tag{2.7}$$

$$n_{eff} = \frac{1}{kd} cos^{-1}\left(\frac{1 - S_{11}^2 + S_{21}^2}{2S_{21}}\right) \tag{2.8}$$

with k, d the respective wavevector, metamaterial's span along z-direction, respectively. After achieving effective refractive index and impedance, permittivity and permeability can be easily retrieved as

$$\epsilon_{eff} = n_{eff}/Z_{eff} \tag{2.9}$$

$$\mu_{eff} = n_{eff} Z_{eff} \tag{2.10}$$

2.4.2 Case 2 : Non-Symmetric behavior of the device

Here, we discussed the method of calculating effective material properties for the devices, which perform differently under forward / backward propagating source. In such a case, we can not take advantage from the symmetry as $S_{11} \neq S_{22}$, so two simulations are performed by illuminating the device from both directions and all four scattering parameters are calculated. Then the following equations are used to retrieve effective properties :

$$n_{eff} = \frac{1}{kd} cos^{-1}\left(\frac{1 - S_{11}S_{22} + S_{21}^2}{2S_{21}}\right) \tag{2.11}$$

$$Z_{eff} = \frac{(T_{22} - T_{11}) \pm \sqrt{(T_{22} - T_{11})^2 + 4T_{12}T_{21}}}{2T_{21}} \tag{2.12}$$

where the elements of transfer (T) matrix used to calculate effective impedance, can be calculated from the S-parameters as :

$$T_{11} = \frac{(1+S_{11})(1-S_{22})+S_{21}S_{12}}{2S_{21}} \tag{2.13a}$$

$$T_{12} = \frac{(1+S_{11})(1+S_{22})-S_{21}S_{12}}{2S_{21}} \tag{2.13b}$$

$$T_{21} = \frac{(1-S_{11})(1-S_{22})-S_{21}S_{12}}{2S_{21}} \tag{2.13c}$$

$$T_{22} = \frac{(1-S_{11})(1+S_{22})+S_{21}S_{12}}{2S_{21}} \tag{2.13d}$$

Then the effective permittivity and permeability can be found in similar way as given by equations 2.9 and 2.10.

2.4.3 Calculating effective material properties of the proposed MIM absorber

In this subsection, we calculated and discussed the effective properties of our proposed system. As our device consists of a multilayer system, where the bottom metallic layer does not let any incident energy to pass through it and we consider it a non-symmetric case to calculate the properties. Two simulations are performed by exciting the metamaterial structure from +z and -z directions. Fig. 2.18 shows the magnitude of all four scattering matrix elements for the absorber. S_{11}, S_{21} are obtained when the system is illuminated with a source propagating from bottom towards top surface and S_{22}, S_{12} for the reverse case. It can be seen from the figure that, when the source is propagating from the bottom side, almost all the light get reflected ($S_{11} \simeq 1$) as its thickness is more than the skin depth, thus no light can even reach to the spacer/top periodic layer, which are responsible of the resonating behavior. However, to see the resonating behavior, one must excited the structure from the top towards bottom.

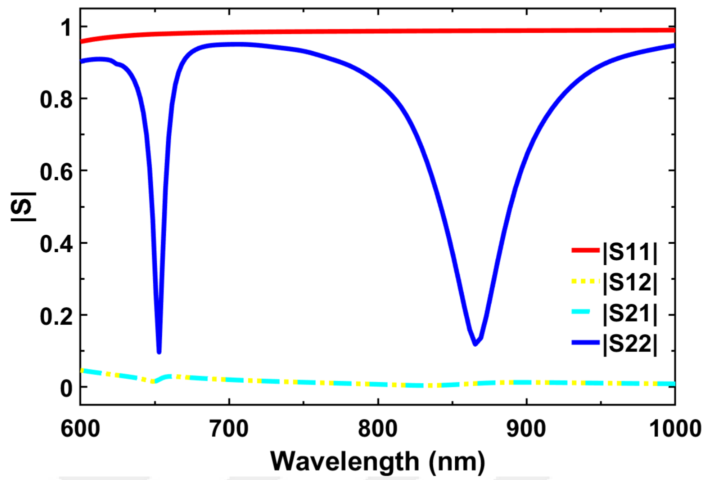

Figure 2.18: Absolute values of the simulated S-parameters for the MIM absorber under study with corresponding device parameters t_B = 100 nm, t_S = t_T = 40 nm, D = 180 nm and periodicity P = 600 nm.

Once, we have these S-parameters, we can easily calculate the effective permittivity, permeability, refractive index and impedance from the method discussed in above section. Fig. 2.19 shows the retrieved effective permittivity, permeability, refractive index, and impedance of the MIM plasmonic absorber which are extracted from the scattering matrix elements using equations 2.9 - 2.13. At the first resonant absorption peak wavelength, permittivity and permeability are found as ϵ_{R1} = 1.04 - 0.02i and μ_{R1} = 1.34 - 0.37i, leading to effective impedance Z_1 = 1.15 - 0.14i. Similarly, for the second peak, these values are calculated as ϵ_{R2} = 1.58 - 0.46i, μ_{R2} = 1.48 + 0.26i, and Z_2 = 0.93 - 0.21i. So, at the resonant frequencies, effective impedance values are almost satisfying the condition of impedance matching with the free space value of $Z_{air} \approx 1$. Hence, the reflection is minimum at these values, and perfect absorption is achieved.

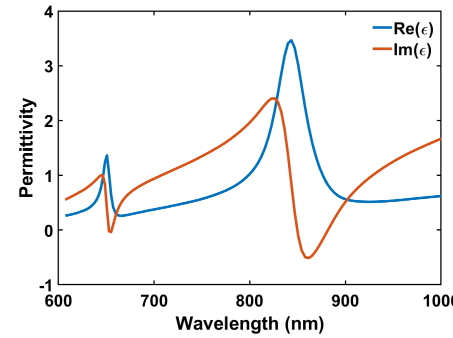

(a)

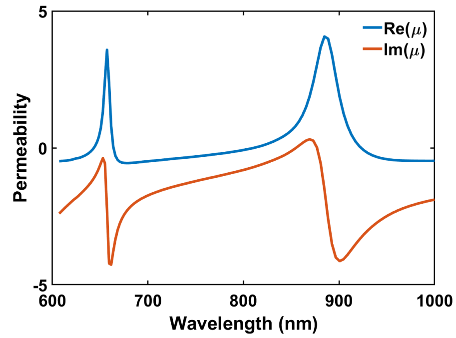

(b)

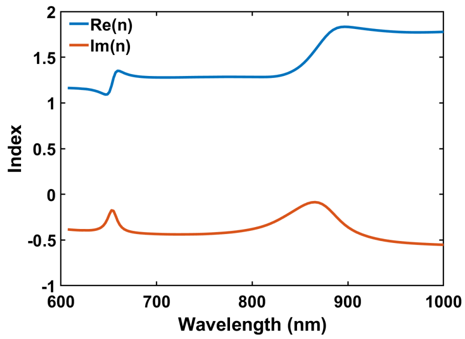

(c)

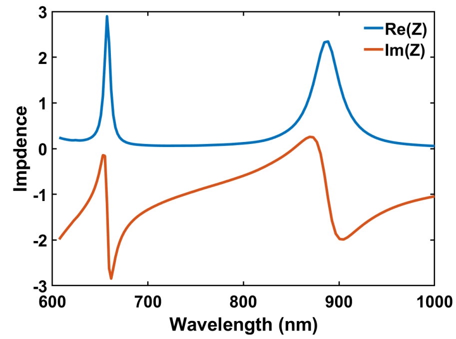

(d)

Figure 2.19: Permittivity (a), Permeability (b), Refractive index (c) and Impedance (d), retrieved from the s - parameters.

2.5 Critical Coupling Phenomenon

Another scenario to explain the perfect absorption is to count the radiative and intrinsic damping rates, γ_r and γ_i, respectively, of the system which becomes equal at the resonant frequencies resulting in the critical coupling (c.c) phenomenon [48, 64]. Middle dielectric spacer plays a critical role and at certain values of t_S (discussed in section 2.3.2.2), these losses become identical around resonant frequencies, resulting in critical coupling and near unity absorption. In this study, we also explained the perfect absorption of our system from the perspective of c.c phenomenon. We calculated the absorption (C_{abs}), scattering (C_{sca})and extinction ($C_{ext} = C_{sca} + C_{abs}$) cross sections using FDTD simulations, presented in Fig. 2.20. It is observed that at the both resonant frequencies (λ_{R1} , λ_{R2}), absorption cross section is almost identical to the scattering cross section i.e. C_{abs}

$\simeq$ C_{sca}, leading to the extinction cross section $C_{ext} \simeq 2C_{sca} \simeq 2C_{abs}$. This occurs whenever the system is in the critical coupling regime such that the radiative and intrinsic rates becomes identical $\gamma_i \simeq \gamma_r$, allowing to achieve near unity absorption. Moreover, it is worthy to mention that at the critical coupling point, absorption and scattering cross sections can exceed the geometrical cross section C_{geo} by an order of magnitude and in this study, we found C_{abs} and C_{scat} around 10-15 times greater than the C_{geo} (= π $(D/2)^2$).

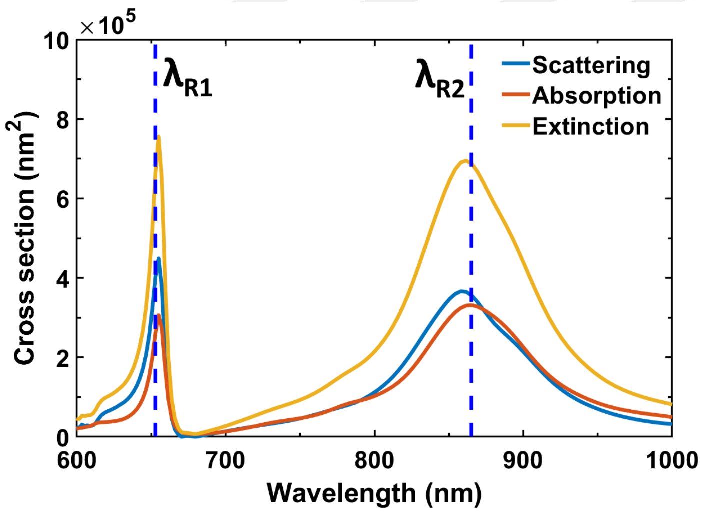

Figure 2.20: Simulated scattering, absorption and extinction (scattering + absorption) cross sections as a function of wavelength for the MIM absorber with optimized structural parameters (t_B = 100 nm, t_S = t_T = 40 nm, D = 180 nm and periodicity P = 600 nm). The vertical blue dashed lines gives the resonant wavelengths (λ_{R1} , λ_{R2}) for both modes, respectively.

2.6 Near Field analysis

In this section, an analysis of the electromagnetic field distributions through the proposed absorber is conducted. To understand the origin of resonant absorption characteristics, electric and magnetic field intensities are computed at resonant wavelengths using frequency domain profile monitor in the Lumerical FDTD solver. These monitors are placed along xz-cross section at y = 0 where the fields intensity is maximum, and cuts through all three layers of the proposed system. The system is excited with an x-polarized plane wave source propagating along z-axis, with device parameters; t_B = 100 nm, t_S = t_T = 40 nm, D = 180 nm and periodicity P = 600 nm .

Fig. 2.21 (a-b) plotted the electric field distribution profiles at the resonant wavelengths of 653nm and 865nm, respectively. Both resonances look like dipole resonance which are excited on the edges of gold nanodisks and the electric field is mainly confined along the boundaries of nanodisks as shown in this figure. However, in case of the first resonance at 653nm, field intensity is enhanced around the top edges at the top nano-unit/air interface, while field is more intense at top nano-unit/dielectric spacer interface for the second resonance at 865nm. In contrast to the electric field distributions which are quite similar for both the resonant modes, magnetic field distribution profiles showed up distinct characteristics as shown in Fig. 2.21 (c-d). In case of the first resonance appearing in the visible region, magnetic field is mostly confined above the nanodisks and between disks in the dielectric spacer/ bottom gold film interface (Fig. 2.21(c)). Meanwhile, this confinement of H-field is much stronger below the nanodisk in spacer region for the second resonance at 870 nm.

From the electric and magnetic field distribution profiles shown in Fig. 2.21 (b, d), we can see that the shorter wavelength resonance appears due to the incident light coupling into the Propagating surface plasmons (PSPs) on the gold film . This resonance clearly follows the periodicity (P) by showing a rapid red-shifting in the absorption peak (Fig. 2.7 a) under grating coupling condition (Equation 1.24) provided by top nanodisks array. On the other hand, the second resonant peak at 865 nm is fundamental localized surface plasmon (LSP) resonance as the magnetic field is mostly confined and localized in the middle dielectric spacer region with no efficient coupling between neighboring nanodisks (Fig. 2.21(d)). This resonant mode shows a rapid red-shifting in response to an increment in nanodisk's diameter ($\mathbf{d}_T$) (Fig. 2.11) but is almost insensitive to the periodicity ($\mathbf{P}$) (Fig. 2.7 a).

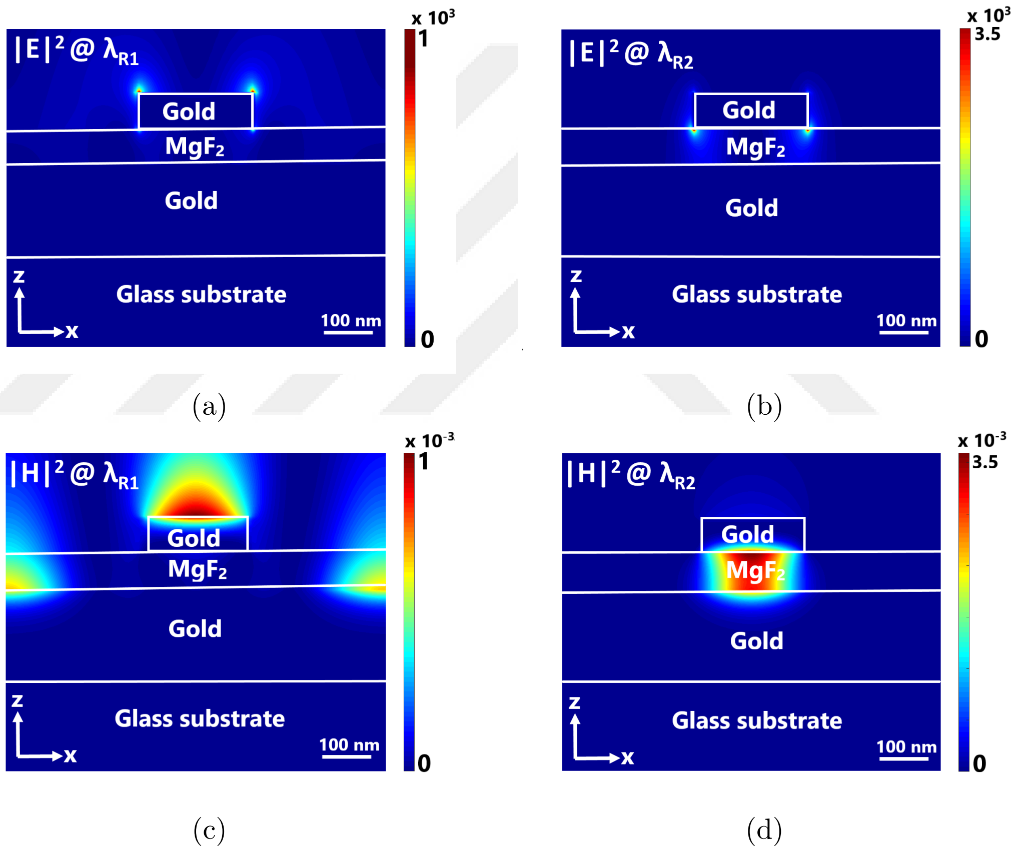

(a) (b)

(c) (d)

Figure 2.21: Cross-sectional view of the simulated electric field intensity $|E|^2$ and magnetic field intensity $|H|^2$ at resonant wavelengths of $\lambda_{R1} \approx 653$ nm (a, c) and $\lambda_{R2} \approx 865$ nm (b, d), respectively. The color bar shows the field enhancements.

2.7 Sensing capabilities of proposed MIM absorber

To analyze the sensing capabilities of the designed MIM absorber, simulations are performed for various values of background refractive index. Plasmonic modes appearing in the absorption spectra are extremely sensitive to surface conditions due to their strong field enhancements and light confinement at subwavelength scale. Consequently, any change in the surrounding environment cause a shift in the resonance peaks. For this purpose, simulations are performed by embedding the proposed structure in dielectric ambiance with refractive index from 1 - 1.25 RIU, with a step of 0.05 RIU. Fig. 2.22(a) shows that a red shift appears in the both resonant peaks as the refractive index is increased. Fig. 2.22(b) plotted the change in resonant wavelengths (Peak1 : blue circle, Peak2 : green diamond) of both the peaks with respect to the refractive index. For peak 1, resonance wavelength linearly follows the refractive index (blue dashed line), and the slope of that linear line defines the refractive index sensitivity which is calculated as ($S_1 \approx 500$). In contrast, second peak's sensitivity is calculated as ($S_2 \approx 235$). Meanwhile, first narrow-band peak shows a ($FOM \approx 34$), almost 11-fold to the second peak giving just a small number($FOM \approx 3$). From these observations, we can say that as the first mode is more exposed to the surrounding environment as the field enhancement for the first resonant mode is along the top edges of the gold disks and it can be affected more easily to any change in the surrounding environment than the second mode where the field is enhanced along the lower edges of nanodisks and is comparatively less sensitive. This causes the first peak to shift more than the second peak at higher wavelength as soon as there is some change happens in the ambiance. Also, the quality factors for the both resonant peaks are calculated as ($Q_1 \approx 44$) and ($Q_2 \approx 11$) , respectively. These results show that the studied Metamaterial absorber is a good candidate for the sensing applications in the designed frequency regime.

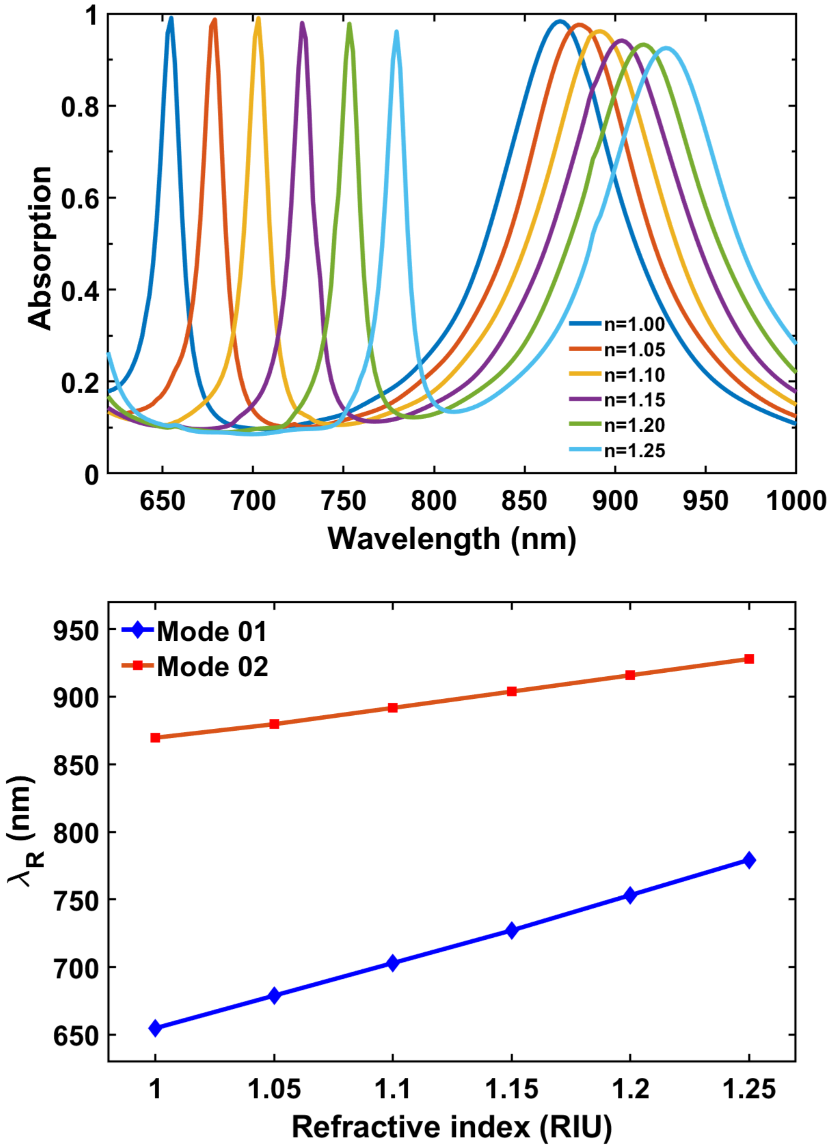

Figure 2.22: (a) Absorption spectra for different values of refractive index. (b) Resonant wavelength as a function of refractive index, with S_1 and S_2 sensitivities of both resonant peaks, respectively.

Chapter 3

Fabrication and Characterization

In this chapter, the fabrication process and tools used to fabricate and characterize the proposed MIM absorber are discussed. For the fabrication, we used the optimized parameters for the system with two different radii of the top nanodisks. The proposed optimal design is composed of 100nm thick gold layer on the glass substrate and a 40nm thick MgF_2 layer as middle dielectric spacer. Top nano-unit is patterned metallic nanodisk with 40nm thickness and two different diameters D = 180, 200 nm. The whole structure is periodic in both x and y axis with the periodicity, P=600.

3.1 Fabriaction process and methods

Fig. 3.1 shows the flow diagram to fabricate proposed MIM absorber. As shown in figure, this nanofabrication process consists of six steps. First of all, an appropriate selection of substrate is made. A square glass substrate is used in this work. In the next step, ground metallic sheet and middle dielectric spacer is deposited using an electron-beam evaporator. Then, to generate a desired pattern the system is covered by a resist (positive or negative) and pattern is formed using various techniques like electron-beam Lithography (EBL), Focused Ion-beam

(FIB) etching and Optical lithography. In this work, EBL is preferred due to its nanometer scale precision. After exposing the sample to E-beam, the pattern is developed by soaking the sample in specific chemicals. Once the pattern is generated, the top metallic layer is deposited again using E-Beam evaporator/Thermal evaporator. In the final step, by employing a lift off method desired pattern is transfered to the sample.

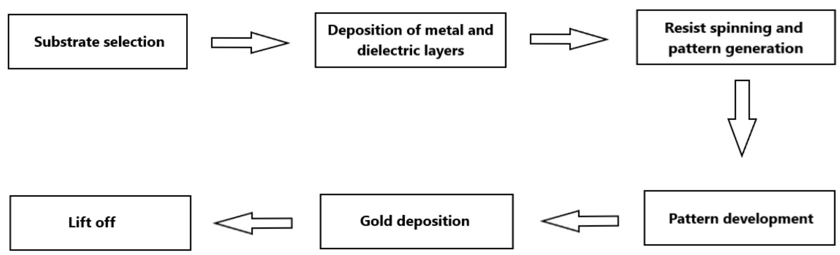

Figure 3.1: Flowchart diagram of fabrication process.

3.1.1 Electron-Beam Evaporation

E-Beam Evaporation is actually a thermal evaporation process, which is used to deposit thin films of various materials. In an E-beam evaporator, the material to be deposit is placed in a crucible. By injecting current to a tungsten filament, it bombards an electron-beam on the source material to evaporate and convert the particles into gaseous state to deposit on the target sample. This all process takes place in the vacuum chamber allowing the vapor atom/molecules to precipitate, thus forming a thin layer on the target sample. For depositions, generally the chamber is set under a vacuum value of $6{\times}10^{-6}$ **torr**. The deposition rate is kept between 0.1-0.3**Å/sec** upto initially 3-5nm of coating, which can be increased upto 1.5**Å/sec** beyond the initial 5nm deposition. The lower deposition rates exhibit better results than the higher rates which may result in non-uniform thickness over the sample substrate. To deposit any metal on glass/silicon substrates, a thin adhesion layer of Titanium is first deposited on the substrate to stick the metal better.

E-beam evaporation has many advantages over other deposition techniques. One of the main advantage is that it produces highly pure films. As only the material is heated without heating the crucible and it is performed inside high vacuum, resulting in just a lower degree of contamination. Also, due to multiple crucible evaporator, many layers of different materials can be deposited simultaneously without breaking the vacuum.

3.1.2 Electron-Beam Lithography

Lithography is a technique used to generate certain designed patterns in a special kind of layer (Resist). Top plasmonic nanostructures are patterned using different etching techniques which depends on the size of desired structure. For example, in higher wavelength regions optical lithography is one of the commonly used microfabrication technique to pattern micron scale structures by exposure of ultraviolet rays. But fundamental diffraction limit does not allow it to pattern the structures at subwavelength scale. However, EBL uses an electronic beam to overcome this diffraction limit and has the capability to realize nanoscale resolution. Due to this reason, EBL is now widely used to pattern nanoscale structures with a precision upto 10nm for a number of plasmonic and metamaterial applications.

EBL is based on scanning a focused electronic beam with designed pattern on an resist covered sample. The resist layer is electron sensitive and usually deposited on the substrate by a spin-coater. There are two types of resists, positive and negative. In EBL system, electron beam is generated by an electron-gun with a tungsten filament and accelerated at high acceleration voltage within a range of 1-100 keV. Then, there is a need to define certain parameters to achieve better exposure to expose the designed patterns. These parameters include; Acceleration voltage, aperture size, writefield size, current, working distance and stepsize.

3.1.3 Lift off process

After doing EBL on the resit layer, a pattern is developed on the layer which is reverse of the designed pattern. Then the final layer is deposited on the sample. To get the designed pattern, sample is soaked in specific chemicals to remove residue of excess resist and material and the technique is known as Lift off.

3.2 Fabrication of MIM plasmonic absorber

In this research work, we proposed a MIM (Gold-MgF_2-Gold) plasmonic absorber with top layer as periodic gold nanodisks showing a narrow-band plasmonic resonance peak in visible and a broad-band plasmonic resonance peak in NIR region. Fig. 3.2 illustrates a schematic diagram of process flow to fabricate MIM absorber with the detailed procedure discussed below

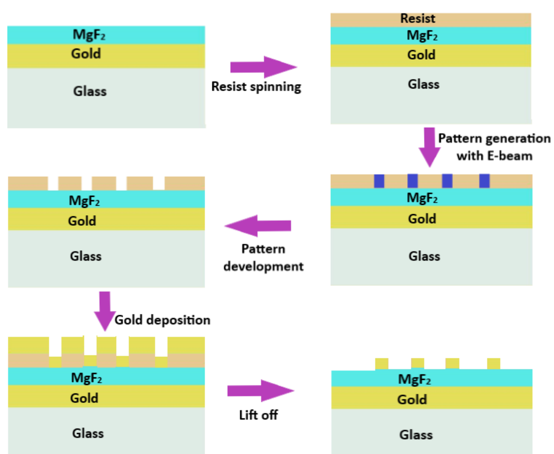

Figure 3.2: A schematic diagram of process flow to fabricate MIM absorber.

1. Gold and MgF_2 deposition: After cleaning the glass sample with IPA (isopropyl alcohol), substrate is deposited with 5nm titanium, 100nm gold and 40nm MgF_2 using a E-beam evaporator. Titanium layer is deposited to enhance the adhesion between glass substrate and gold film. The deposition is operated at a pressure around $5{\times}10^{-6}$ **Torr** and deposition rates of 0.2, 0.9 and 1 **Å/sec** are used to deposit Ti, Au and MgF_2 layers.

2. Spin coating of Resist layer: To deposit top patterned periodic array, a resist layer is coated on the sample using a spin coater. Bilayer process has been performed to have easy liftoff. The sample is spin-coated with a 495 PMMA C2 at 4000 rpm for 50 seconds and baked at 170^0C for 2 minutes on a hot plate. Then, 950 PMMA C2 is spin-coated with the same parameters on top of the first layer and baked at the same conditions. Total PMMA thickness is around $\sim$ 200nm ($\sim$ 100nm+100nm).

3. Pattern generation with EBL exposure: Once the sample is coated with bilayer PMMA resist, the desired pattern is generated by EBL exposure. Patterns are processed through a special program called BEAMER form GenISys Company with including 200nm PMMA Proximity Effect Correction(PEC) module and adjust the resolution with 2nm Spot Size / Distance parameters suitable with our EBL system Vistec/Raith EBPG 5000+ES. Exposure is performed with 0.5**nA** at 100**kV** with 700 $\mu\mathbf{C/cm}^2$ Dose.

4. Pattern development: The sample is developed by soaking in 1:3 (MIBK:IPA) solution for 1 minute followed by rinsing with IPA for 15 seconds and then dried with nitrogen gas. A very short (5 seconds) Oxygen plasma is performed to get rid of any possible remained PMMA residues on the developed regions.

5. Metal deposition: 3nm Ti and 40nm gold are deposited on the patterned sample using E-beam evaporator with deposition rates of 0.2 and 0.9**Å/sec**.

6. Lift off and plasma cleaning: Sample is soaked in acetone solution placed on a hot plate at 80^0C for 30 minutes and rinsed by IPA for 60 seconds to remove unnecessary resist and residue metal particle. Finally, the sample is ready with the designed MIM structure. Despite the lift off process, some residue of resist are left on the sample and an oxygen plasma cleaning is performed for 20 minutes to get the final structure.

3.3 Characterization of MIM absorber

In this section, a brief discussion is provided to describe the process and tools used to characterize the fabricated MIM absorber. A Stylus Profilometer is used to measure the thickness of MIM layers. To visualize and check the consistency of designed and fabricated device's geometrical parameters, scanning electron microscopy(SEM) is used.

3.3.1 Measuring thickness with Stylus Profilometer

Profilometry is a technique adopted to extract topological information from a surface. It is generally used to measure height variations and surface roughness. These measurement are made via two methods by using light (Optical Profilometer) or a physical prob (Stylus Profilometer). A Stylus profilometer involves a physical movement of probe(Stylus) in all three direction which needs a force feedback and gives high z resolution. After depositing Ti-Au-MgF_2 (5-100-40nm) on the glass substrate, thickness of these layers is measured with a Stylus profilometer which gives the total thickness around ∼151nm (Fig. 3.3) with a difference of few nanometers from the expected 145nm thickness.

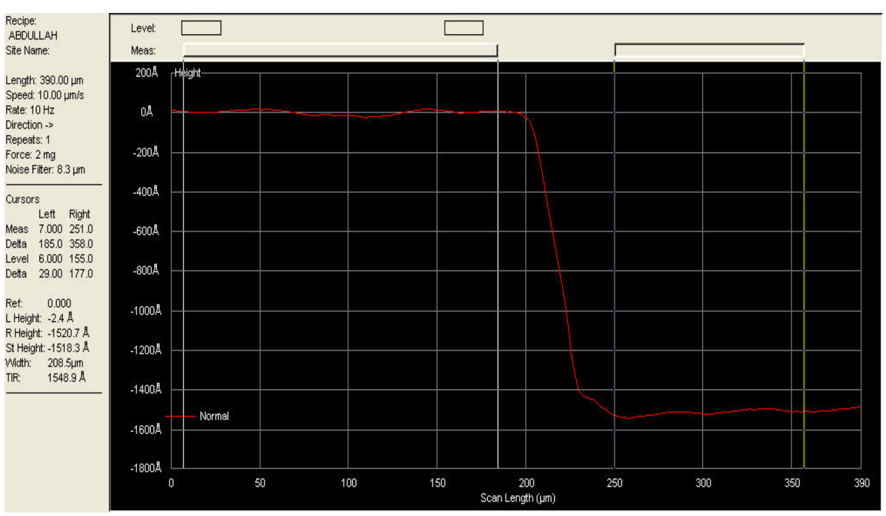

Figure 3.3: Thickness of the Ti-Au-MgF_2 stack measured with a Stylus profilometer.

3.3.2 SEM Measurements

Scanning electron microscope is used to visualize any sample surface by scanning a focused beam of accelerated electrons and detecting secondary, backscattered electrons simultaneously. In this technique, sample is placed in vacuum and electrons are bombard on the sample from an electron gun. Then through detection of backscattered electrons, secondary electrons and x-rays, signals are produced. An analysis of secondary electrons produce a topographic image, while backscattered electrons generates an image based on mass of the elements. In contrast to any optical microscope which creates any image with a resolution around $\sim$200 μm,an SEM image can have resolution of $\sim$10 nm. We used SEM to visualize and determine the geometrical dimensions of the top nanodisks layer of fabricated MIM absorber. Fig. 3.4 shows the images taken from SEM for nanodisk with two different radii 90nm (a,b) and 100nm (c,d). It can be observed from the figure that nanodisks have almost round shape and a well distributed square lattice.

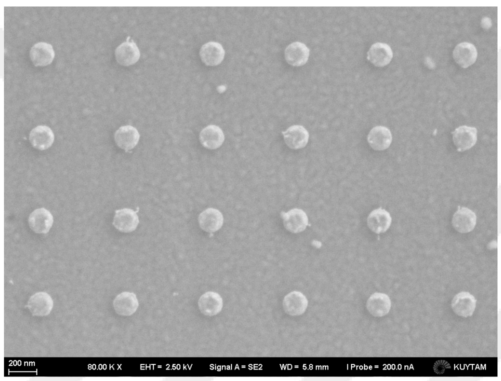

(a)

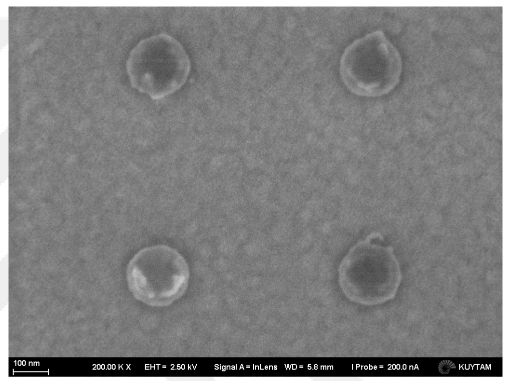

(b)

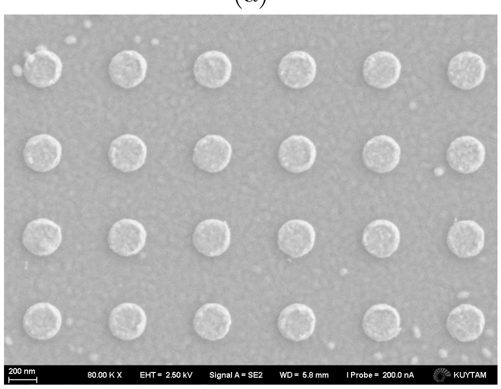

(c)

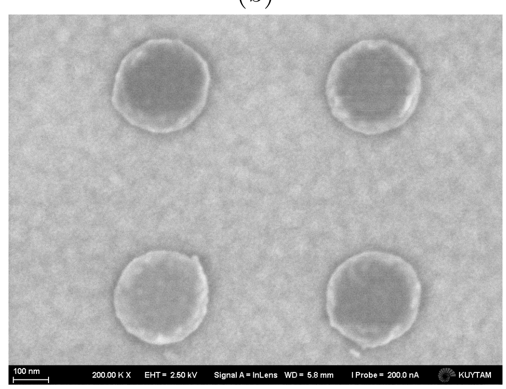

(d)

Figure 3.4: SEM images(Top view) of top nanodisks with radii 90nm (a-b) and 100nm (c-d).

Chapter 4

Plasmonic nanoantennas for a Cr:ZnSe laser

In this chapter, a discussion is made on an ongoing project to check a homemade tunable Cr:ZnSe laser in the infrared region lasing around 2200-2700 nm, with monolayer plasmonic gold nanoantennas.

4.1 Optical Setup

Optical setup consists of two parts as shown in Fig. 5.1. In the first part, Tm fiber laser pump is used to pump a beam of wavelength around 1.8 μm, which passes through a curved mirror and excites a Cr:ZnSe crystal, resulting in beam of infrared light which is dispersed into different wavelengths between 2200-2700 nm using a prism and high reflector. To measure the wavelength of laser beam, it is passed through several mirrors and with the help of a movable mirror, it is transferred to an APE spectrometer which gives information about exact wavelength and bandwidth of the signal and by properly tuning the high reflector, wavelength is adjusted. To characterize the sample, movable mirror is moved away from the path of laser beam, and with the aid of another mirror, it

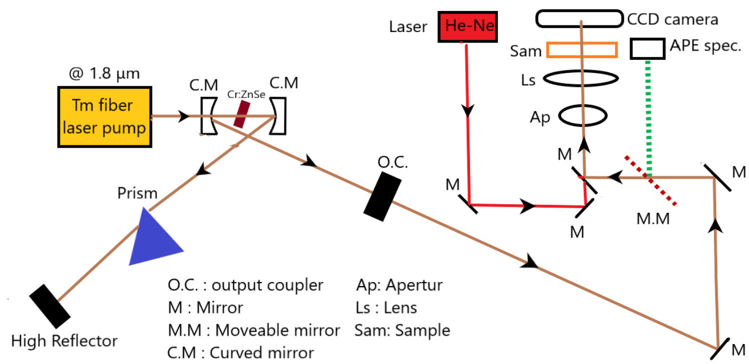

Figure 4.1: A schematics of the optical setup consisting of two parts. One part is related to the tunable Cr:ZnSe laser lasing between 2200-2700 nm. Second part is for the characterization of sample. Credit to Laser research laboratory, Koç University, Istanbul.

strikes the sample placed on a translational stage sample holder passing through an aperture and lens. As we want to focus on particular points on the sample, we need to look the beam spot on the sample with the help of charged coupled device (CCD) camera. But as laser is operating in the IR range, the spot can not be observed. To overcome this problem, an He-Ne laser lasing in the visible region is used and with the help of couple of mirrors, its light beam is overlapped with the IR beam, which results in showing the laser spot on the sample. Then to measure the reflectance or transmission, a power meter is placed before and after the sample for each data point.

4.2 Designing and Fabrication of Plasmonic nanoantennas

To check the laser system, we designed and simulated plasmonic monolayer gold nanoantennas with different shapes and geometries on a CaF_2 substrate. These nanoantennas are designed in such way that plasmonic resonances can be excited within the operating region of our laser setup. For the simulations, same FDTD method is employed using a commercial Lumerical software. Fig. 5.2 shows four

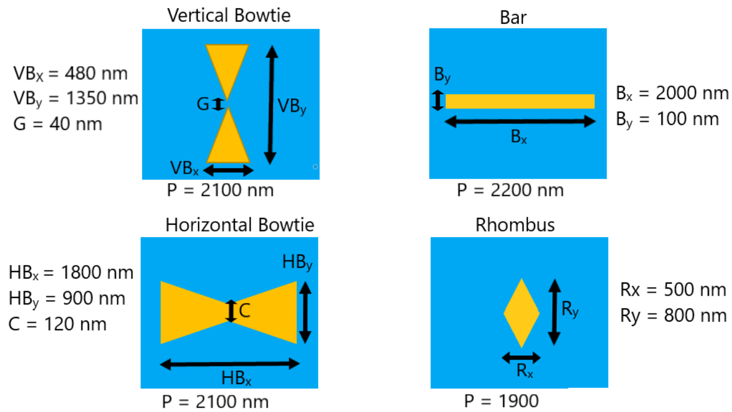

Figure 4.2: Schematics of four different types of nanoantennas with their structural parameters. These structures are periodic in lateral directions with periodicity P.

different types of periodic nanoantennas with corresponding structural parameters. All nanoantennas are composed of gold with thickness $t_G = 40$ nm.

In the next step, the designed nanostructures are fabricated using standard nanofabrication techniques. In the first step, a PMMA layer is deposited on CaF_2 substrate and the designed structures are patterned. Each structure is spread in x and y direction within area of 200×200 μm. Then, a thermal evaporator used to deposit gold on the desired structures followed by a standard lift-off process. Finally, the required nanoantennas are achieved. To visualize the fabricated sturctures, scanning electron microscope is used. Fig. 5.3 depicts SEM images for all four kind of periodic gold nanoantennas and all are in well agreement with the designed shapes and structural parameters.

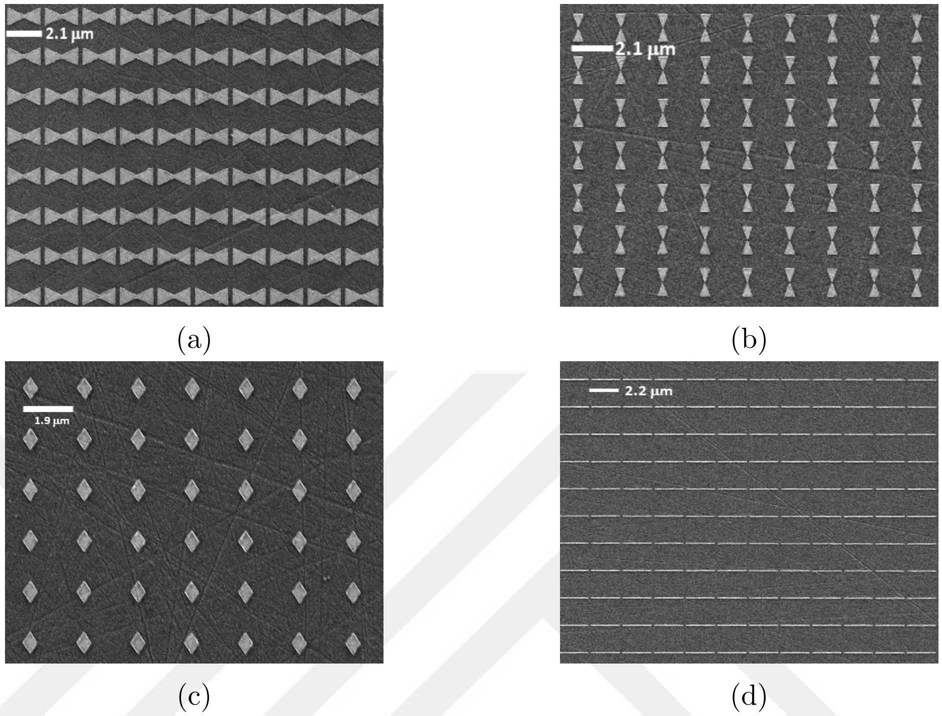

(a) (b) (c) (d)

Figure 4.3: SEM images of horizontal bow-tie(a), Vertical bow-tie(b), rhombus (c) and bar (d), shaped nanoantennas.

4.3 Optical measurements

The designed nanostructures are simulated using FDTD simulations and resulting reflection spectra is shown in Fig. 5.4 (a). All four nanoantennas are resonating between our desire wavelength range where the laser system is lasing i.e. around 2200-2400 nm. We have got our initial results where one of the structure's is showing resonance behavior around 2300 nm with reflection reaching to almost 0.4. However, due to fluctuations in the laser beam there are some discrepancies, as we are dealing with the homemade laser and it's quite challenging to get the results easily. But, we expect more compatible results, still to come.

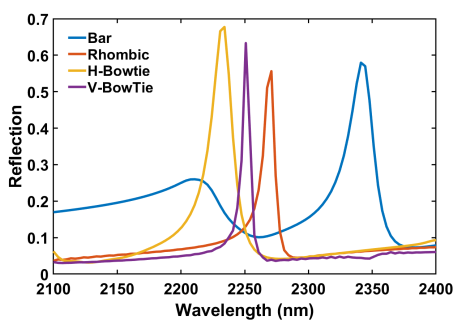

(a) Simulations

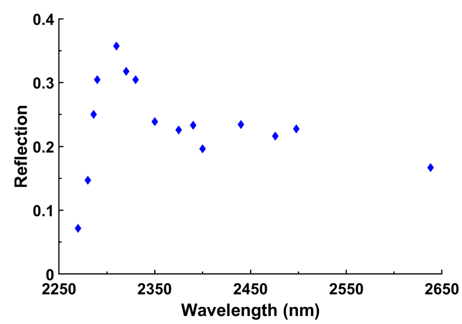

(b) Laser measurement

Figure 4.4: Reflection spectra of the fabricated nanostructures using (a) FDTD simulations, (b) Cr: ZnSe laser setup.

Chapter 5

Conclusion and Future Direction

In this thesis, we numerically investigated and fabricated a dual-band perfect absorber at visible-near-infrared frequencies. This project is carried through a cycle of four steps; Designing, simulation, fabrication and characterization, respectively. For designing and simulations, FDTD simulations were performed using Lumerical software. To produce optimum results (narrow band and perfect absorption), numerous simulation were carried out to optimize the design and structural parameters of the proposed device. An analysis is made to describe the device performance for these structural parameters : top metal layer thickness (t_T), dielectric spacer thickness (t_S), addition of top metal nanodisk's and its diameter (D), and array pitch constant (P). Polarization dependence was also investigated, which did not give any noticeable results as the top periodic disks behave similarly to any polarized source due to its circular symmetry. Also the effect of material used for the composition of perfect absorber is demonstrated by applying a sweep on the refractive indices of the middle dielectric spacer and for three different metals (Gold, Silver and Aluminum). The proposed design is optimized for dual-narrow band characteristics achieving perfect absorption and high sensitivity. Two narrow band peaks showed up in the absorption spectra of the system reaching almost 100 % absorption efficiency, and the physical origin of these peaks was found to be the excitation of two different plasmonic resonances (Localized and propagating). To explain the perfect absorption of the system through impedance matching and critical coupling phenomenons, FDTD simulation were performed to calculate scattering matrix elements (S-parameters) and cross sections. Finally, sensing capabilities of the MIM absorber were analyzed by calculating Sensitivity, Figure of merit and quality factors of the resonance modes.

After successfully optimizing the device parameters, it was fabricated using various nanofabrication techniques. E-beam evaporator was used to coat the bottom metal and dielectric layers on a glass substrate. In the next step, sample was covered with a bi-layer PMMA using a spin coater and patterned (circular nanodisks) by E-beam lithography. Finally, gold was deposited on the developed sample by a thermal evaporator and a lift-off process performed to obtain the final structure.

For the characterization of the fabricated sample, Profilometer and SEM (scanning electron microscopy) were used. A stylus profilometer was used to measure the thickness of the metal/dielectric layers. To visualize the fabricated MIM device and to determine the dimension of the top periodic nanodisks, an SEM tool was used and images were taken.

In a nutshell, this research study analyzes the perfect absorption phenomenon in MIM based PA in detail and in the community of PAs it will be a go to guide for the researchers. In Future, we will apply our methodology to explain perfect absorption phenomenon in similar kind of nanostructures operating at infrared frequencies.

Bibliography

[1] Stefan A. Maier, "Plasmonics: Fundamentals and Applications," *Springer*, 2007.

[2] Ekmel Ozbay, "Plasmonics: Merging Photonics and Electronics at Nanoscale Dimensions," *E. Science* 311, 189-193,2006.

[3] S. R. K. Rodriguez, A. Abass, B. Maes, O. T. A. Janssen, G. Vecchi, and J. Gomez Rivas, "Coupling Bright and Dark Plasmonic Lattice Resonances," *Phy. Rev. X* 1, 021019, 2011.

[4] Yuchan Du,Lina Shi, Meihua Hong, Hailiang Li,Dongmei Li,Ming Liu, "A surface plasmon resonance biosensor based on gold nanoparticle array," *Opt. Com.* 298299, 232236, 2013.

[5] Suo Wang, Hua-Zhou Chen, and Ren-Min Ma, "High Performance Plasmonic Nanolasers with External Quantum Efficiency Exceeding 10

[6] Jacek Gosciniak, Fatih B. Atar, Brian Corbett, and Mahmoud Rasras, "Plasmonic Schottky photodetector with metal stripe embedded into semiconductor and with a CMOScompatible titanium nitride," *Sci. Rep.* 9:6048, 2019.

[7] Tae-Woo Lee, Da Eun Lee, and Soon-Hong Kwon, "Dual-Function Metal-InsulatorMetal Plasmonic Optical Filter," *IEEE Photonics Journal* 7(1):1-8, 2015.

[8] Yoav Avitzour, Yaroslav A. Urzhumov, and Gennady Shvets, "Wide-angle infrared absorber based on a negative-index plasmonic metamaterial," *Phys. Rev. B* 79, 045131, 2009.

[9] Rodger M. Walser, "Electromagnetic metamaterials," *Proc. SPIE* 4467, 2001.

[10] S. Haxha, F.Abdel Malek, F. Ouerghi, M. D. B. Charlton, A. Aggoun, and X. Fang, "Metamaterial Superlenses Operating at Visible Wavelength for Imaging Applications," *Sci. Rep.* 8:16119, 2018.

[11] Ben Wood, "Metamaterials and invisibility," *Comptes Rendus Physique* 10(5):379-390, 2009.

[12] J.Y. Rhee, Y.J. Yoo, K.W. Kim, Y.J. Kim, and Y.P. Lee, "Metamaterial-based perfect absorbers," *Journal of Electromagnetic Waves and Applications* 28:13, 1541-1580, 2014.

[13] N. I. Landy, S. Sajuyigbe, J. J. Mock, D. R. Smith, and W. J. Padilla, "Perfect Metamaterial Absorber ," *Phy. Rev. Lett.* 100, 207402, 2008.

[14] Furkan Dincer, Mehmet Bakir, Muharrem Karaaslan, Kemal Delihacioglu, Cumali Sabah, "Perfect Metamaterial absorber based energy harvesting application in ISM Band ," *UBT International Conference* 91, 2015.

[15] Zenghui Xu, Dong Wu, Yumin Liu, Chang Liu, Zhongyuan Yu, Li Yu, and Han Ye, "Design of a Tunable Ultra-Broadband Terahertz Absorber Based on Multiple Layers of Graphene Ribbons ," *Nanoscale Res Lett.* 13:143, 2018.

[16] Shiwen Luo, Jun Zhao, Duluo Zuo, and Xinbing Wang, "Perfect narrow band absorber for sensing applications ," *Opt. Exp.* 24(9), 9288-9294, 2016.

[17] E. Aslan, E. Aslan, M. Turkmen, O.G. Saracoglu, "Metamaterial plasmonic absorber for reducing the spectral shift between near- and far-

eld responses in surface enhanced spectroscopy applications," *Sens. Actuators A* 267, 60-69, 2017.

[18] E. Aslan, E. Aslan, M. Turkmen, O.G. Saracoglu, "Experimental and numerical characterization of a mid-infrared plasmonic perfect absorber for dual-band enhanced vibrational spectroscopy," *Opt. Mat.* 73, 213-222., 2017.

[19] H. Tao, C.M. Bingham, A.C. Strikwerda, "Highly flexible wide angle of incidence terahertz metamaterial absorber: Design, fabrication, and characterization," *Phys. Rev. B* 78, 241103, 2008.

[20] X.P. Shen, T.J.Cui, J.M. Zhao, "Polarization-independent wide-angle triple-band metamaterial absorber," *Opt. Exp.* 19, 94019407, 2011.

[21] L. Zhao, H. Liu, Z.H. He, "Design of multi-narrowband metamaterial perfect absorbers in near-infrared band based on resonators asymmetric method and modified resonators stacked method," *Opt. Commun.* 420, 95103, 2018.

[22] Shinpei Ogawa, and Masafumi Kimata, "Metal-Insulator-Metal-Based Plasmonic Metamaterial Absorbers at Visible and InfraredWavelengths: A Review," *Materials* 11, 458, 2018.

[23] H. Raether, "Surface Plasmons on Smooth and Rough Surfaces and on Gratings," *springer-Verlag*, 1988.

[24] P. Andrew, W. L. Barnes, "Energy Transfer Across a Metal Film Mediated by Surface Plasmon Polaritons," *Science* 306 (5698), 1002, 2004.

[25] P. Zheng, "Plasmon-Enhanced Optical Sensing by Engineering Metallic Nanostructures," *Graduate Theses, Dissertations, and Problem Reports* 3710, 2010.

[26] L. Novotny and B. Hecht, "Surface plasmon polaritons at plane interfaces," *Principles of Nano-Optics, Cambridge University Press* 382-386, 2006.

[27] E. Plum, "Chirality and Metamaterials," 2010.

[28] A. Sihvola, "Metamaterials in electromagnetics," *Metamaterials* 1, 2-11, 2007.

[29] T. J. Cui, D. Smith, and R. Liu, "Metamaterials: Theory, Design, and Applications," *Springer*, 2009.

[30] D. R. Smith, W. J. Padilla, D. C. Vier, R. Shelby, S. C. Nemat-Nasser, N. Kroll, and S. Schultz, "Left-Handed Metamaterials," *Soukoulis C.M. (eds) Photonic Crystals and Light Localization in the 21st Century. NATO Science Series (Series C: Mathematical and Physical Sciences), vol 563. Springer, Dordrecht*, 2001.

[31] N. Mattiucci, M. J. Bloemer, N. Akzbek, and G. D'Aguanno, "Impedance matched thin metamaterials make metals absorbing," *Sci. Rep.*, 3:3203, 2013.

[32] Na Liu, Martin Mesch, Thomas Weiss, Mario Hentschel, and Harald Giessen, "Infrared Perfect Absorber and Its Application As Plasmonic Sensor," *Nano Lett.*, 10, 2342-2348, 2010.

[33] G. Kenanakis,Ch. P. Mavidis, E. Vasilaki, N. Katsarakis, M. Kafesaki, E. N. Economou, and C. M. Soukoulis, "Perfect absorbers based on metal-insulator-metal structures in the visible region: a simple approach for practical applications," *Applied Physics A*, 123:77, 2017.

[34] Fei Ding, Jin Dai, Yiting Chen, Jianfei Zhu, Yi Jin, and Sergey I. Bozhevolnyi, "Broadband near-infrared metamaterial absorbers utilizing highly lossy metals," *Sci. Rep.*, 6:39445, 2016.

[35] Chenggang Hu, Zeyu Zhao, Xunan Chen, and Xiangang Luo, "Realizing near-perfect absorption at visible frequencies," *Opt. Exp.*, 17(13), 11039-11044, 2009.

[36] Imre Ozbay, "Design, Fabrication And Characterization of an Ultra-Broadband Metamaterial Absorber using Bismith in Near Infrared region," *Master of Science Thesis, Middle East Technical University, Turkey*, 2018.

[37] Y. H. Liu, S. Gu, C. R. Luo, and X. P. Zhao, "Ultra-thin broadband metamaterial absorber," *Appl. Phys., A Mater. Sci. Process*, 2012.

[38] J. Grant, Y. Ma, S. Saha, A. Khalid, and D. R. S. Cumming, "Polarization insensitive, broadband terahertz metamaterial absorber," *Opt. Lett.* 36(17), 3476-3478, 2011.

[39] X. Ni, Z.J. Wong, M. Mrejen, Y. Wang, X. Zhang, "An ultrathin invisibility skin cloak for visible light," *Science* 349, 1310-1314, 2015.

[40] Z. Qian, S. Kang, V. Rajaram, C. Cassella, N.E. McGruer, M. Rinaldi, "Zero-power infrared digitizers based on plasmonically enhanced micromechanical photoswitches," *Nat. Nanotechnol.* 12, 969-973, 2017.

[41] H.-H. Chen, Y.-C. Su, W.-L. Huang, C.-Y. Kuo, W.-C. Tian, M.-J. Chen, S.-C. Lee, "A plasmonic infrared photodetector with narrow bandwidth absorption," *Appl. Phys. Lett.* 105, 2014.

[42] H.T. Miyazaki, T. Kasaya, M. Iwanaga, B. Choi, Y. Sugimoto, K. Sakoda, "Dual-band infrared metasurface thermal emitter for CO2 sensing," *Appl. Phys. Lett.* 105, 2014.

[43] Junqiao Wang, Chunzhen Fan, Pei Ding, Jinna He, Yongguang Cheng, Weiqin Hu, Genwang Cai, Erjun Liang1, and Qianzhong Xue, "Tunable broad–band perfect absorber by exciting of multiple plasmon resonances at optical frequency," *Opt. Exp.*, 20(14), 14871-14878, 2012.

[44] M. D. Gold am, E. A. Kadlec, B. V. Olson, J. F. Klem, S. D. Hawkins, S. Parameswaran, W. T. Coon, G. A. Keeler, T. R. Fortune, A. Tauke-Pedretti, J.R. Wendt, E. A. Shaner, P. S. Davids, J. K. Kim, and D. W. Peters, "Enhanced infrared detectors using resonant structures combined with thin type-II super lattice absorbers," *Appl. Phys. Lett.* 109(25), 251103, 2016.

[45] C. Argyropoulos, K. Q. Le, N. Mattiucci, G. D'Aguanno, and A. Alu, "Broadband absorbers and selective emitters based on plasmonic Brewster metasurfaces," *Phys. Rev. B* 87(20), 205112, 2013.

[46] J. P. Guo, Y. Zou, H. S. Leong, and B. Y. Zhang, "Multiplexed Nanostructure Metamaterial for Wide Spectral and Perfect Light Absorption," *Photonic Metamaterials and Plasmonics, OSA Technical Digest (CD), paper MWB4*, 2010.

[47] Lei Lei, Shun Li, Haixuan Huang, Keyu Tao, Anf Ping Xu, "Ultra-broadband absorber from visible to near-infrared using plasmonic metamaterial," *Opt. Exp.*, 26(5), 5686-5693, 2018.

[48] Kai Chen, Ronen Adato, and Hatice Altug, "Dual-Band Perfect Absorber for Multispectral Plasmon-Enhanced Infrared Spectroscopy," *ACS Nano*, 6(9), 7998-8006, 2012.

[49] Yizhuo Chu, Mohamad G. Banaee, and Kenneth B. Crozier, "Double-Resonance Plasmon Substrates for Surface-Enhanced Raman Scattering with Enhancement at Excitation and Stokes Frequencies," *ACS Nano* , 4, 5, 2010.

[50] Khai Q. Le, Quang Minh Ngo, and Truong Khang Nguyen , "Nanostructured Metal-Insulator-Metal Metamaterials for Refractive Index Biosensing Applications: Design, Fabrication, and Characterization," *IEEE Journal Of Selected Topics In Quantum Electronics*, 23(2), 2017.

[51] Xiaoyuan Lu, Rengang Wan, and Tongyi Zhang, "Metal-dielectric-metal based narrow band absorber for sensing applications," *Opt. Exp.*, 23(23), 29842-29847, 2015.

[52] Chen Chen, Guan Wang, Ziyang Zhang, and Kai Zhang, "Dual narrow-band absorber based on metal-insulator-metal configuration for refractive index sensing," *Opt.Lett.*, 43(15), 3630-3633, 2018.

[53] Shiwen Luo, Jun Zhao, Duluo Zuo, and Xinbing Wang, "Perfect narrow band absorber for sensing applications," *Opt. Exp.*, 24(9), 9288-9294, 2016.

[54] Ming Zhang, Jiawen Fang, Fei Zhang, Junyan Chen, and Honglin Yu, "Ultra-narrow band perfect absorbers based on Fano resonance in MIM metamaterials," *Opt. Comm.*, 405, 216-221, 2017.

[55] Lijun Meng, Ding Zhao, Zhichao Ruan, Qiang Li, Yuanqing Yang, and Min Qiu, "Optimized grating as an ultra-narrow band absorber or plasmonic sensor," *Opt. Lett.*, 39(5), 2014.

[56] Zhongyang Li, Serkan Butun, and Koray Aydin, "Ultranarrow Band Absorbers Based on Surface Lattice Resonances in Nanostructured Metal Surfaces," *ACS Nano*, 8(8), 82428248, 2014.

[57] K. Aydin, V.E. Ferry, R.M. Briggs, H.A. Atwater, "Broadband polarizationindependent resonant light absorption using ultrathin plasmonic super absorbers," *Nat. Commun.* 2, 517, 2011.

[58] T. Maier, H. Brueckl, "Multispectral microbolometers for the midinfrared," *Opt. Lett.* 35, 37663768, 2010.

[59] S.Thongrattanasiri, F.H.L. Koppens, F.J. Garcia de Abajo, "Complete Optical Absorption in Periodically Patterned Graphene," *Phys. Rev. Lett.* 108, 2012.

[60] K. Gorgulu, A. Gok, M. Yilmaz, K. Topalli, N. Biyikli, A.K. Okyay, "All-Silicon Ultra-Broadband Infrared Light Absorbers," *Sci. Rep.* 6, 2016.

[61] A. Lefebvre, D. Costantini, I. Doyen, Q. Lievesque, E. Lorent, D. Jacolin, J.J. Greffet, S. Boutami, H. Benisty, "CMOS compatible metal-insulator-metal plasmonic perfect absorbers," *Opt. Mater. Exp.* 6, 2389-2396, 2016.

[62] D. Hasan, P. Pitchappa, J.Wang, T.Wang, B. Yang, C.P. Ho, C. Lee, "Novel CMOS-Compatible MoAlNMo Platform for Metamaterial-Based Mid-IR Absorber," *ACS Photonics* 4, 302-315, 2017.

[63] Xianliang Liu, Tatiana Starr, Anthony F. Starr, and Willie J. Padilla, "Infrared Spatial and Frequency Selective Metamaterial with Near-Unity Absorbance," *Phy. Rev. Lett.*, 104, 207403, 2010.

[64] Rasoul Alaee, Mohammad Albooyeh, and Carsten Rockstuhl, "Theory of metasurface based perfect absorbers," *J. Phys. D: Appl. Phys.*, 50, 503002, 2017.

[65] www.Lumerical.com

[66] Edward D. Palik, "Handbook of Optical Constants of Solids Vol. 3," 1998.

[67] D. R. Smith, D. C. Vier, Th. Koschny, and C. M. Soukoulis, "Electromagnetic parameter retrieval from inhomogeneous metamaterials," *Phy. Rev. E* , 71, 036617, 2005.

Appendix A

Data

Appendix B

Code